Published in final edited form as:

SIAM J Appl Math. 2022 ; 82(1): 267–293. doi:10.1137/21m1401024.

DEVELOPMENT OF FIBRIN BRANCH STRUCTURE BEFORE AND AFTER GELATION*

AARON L. FOGELSON[†], **ANNA C. NELSON**[‡], **CHERYL ZAPATA-ALLEGRO**[§], **JAMES P KEENER**[¶]

[†]Departments of Mathematics and Biomedical Engineering, University of Utah, Salt Lake City, UT (http://www.math.utah.edu/~fogelson).

[‡]Department of Mathematics, University of Utah, Salt Lake City, UT.

[§]Department of Mathematics, University of Utah, Salt Lake City, UT.

[¶]Departments of Mathematics and Biomedical Engineering, University of Utah, Salt Lake City, UT (http://www.math.utah.edu/~keener).

Abstract

In [Fogelson and Keener, *Phys. Rev. E*, 81 (2010), 051922], we introduced a kinetic model of fibrin polymerization during blood clotting that captured salient experimental observations about how the gel branching structure depends on the conditions under which the polymerization occurs. Our analysis there used a moment-based approach that is valid only before the finite time blow-up that indicates formation of a gel. Here, we extend our analyses of the model to include both pre-gel and post-gel dynamics using the PDE-based framework we introduced in [Fogelson and Keener, *SIAM J. Appl. Math.*, 75 (2015), pp. 1346–1368]. We also extend the model to include spatial heterogeneity and spatial transport processes. Studies of the behavior of the model reveal different spatial-temporal dynamics as the time scales of the key processes of branch formation, monomer introduction, and diffusion are varied.

Keywords

kinetic gelation; blood clotting; fibrin branching; gel front; generating function; polymer diffusion

AMS subject classifications.

92C05; 92C45; 82C26; 82D60

1. INTRODUCTION.

The formation of a fibrin gel, or fibrin clot, is an important component of the blood clotting process; it complements the other major part of the clotting process, platelet aggregation [11]. Together, clumps of platelets and a fibrin mesh between and around the platelets

*Submitted to the editors September 20, 2021.

fogelson@math.utah.edu .

constitute the bulk of many blood clots. The structure of the fibrin clot (branch points per unit volume, fiber thickness, pore sizes, etc.) is sensitive to the conditions under which the gel is formed. Both the mechanical properties of the clot and the efficacy of clot degradation by the fibrinolytic system [21] are very sensitive to its structure. Variations in clot structure are correlated with bleeding or thrombotic disorders [6, 8, 24].

Fibrin clots are assembled from fibrin protofibrils which are in turn composed of fibrin monomers produced by the action of the enzyme thrombin on the plasma protein fibrinogen (as reviewed [23]). Briefly, fibrinogen is an elongated, trinodular molecule with a central E region connected by coiled-coil chains to two D regions. As illustrated in Fig. 1, a fibrin monomer is produced when thrombin cleaves two short protein fragments, called fibrinopeptides, from the E region on fibrinogen. This uncovers two “A” sites, each of which can bind to a constitutively-exposed complementary “a” site in the D region of another fibrin(ogen) molecule. Through this binding process, fibrin monomers spontaneously polymerize into long double-stranded protofibrils that are half-staggered through middle to end binding. When sufficiently long, the double-stranded protofibrils can bind side by side to form thicker fibers in a process known as lateral assembly. Somewhere during the formation of a protofibril and/or during lateral assembly branches form and, eventually, a three-dimensional fibrin gel results.

The fibrin branching is not well understood. There is no specific molecule responsible for nucleating branch formation; in fact, a three dimensional gel can develop *in vitro* in a solution in which the only proteins present are fibrinogen and thrombin [20]. Experimental results indicate that the thrombin concentration strongly influences the structure of the gel that forms [1, 20]. High thrombin concentrations result in “fine” clots, with relatively thin fibers, a high volume density of branch points, and small pore size. Low thrombin concentrations produce “coarse” clots: thicker fibers, lower branch point density, and larger pores [20]. During clotting *in vivo*, thrombin is produced on the surfaces of platelets in the platelet aggregates and is then released into the surrounding fluid where it can convert fibrinogen to fibrin monomers. In *in vitro* studies in which thrombin is produced by reactions on cellular surfaces [2, 3, 21], the structure of the resulting fibrin clots varies with distance from the cell surfaces. A fine gel is seen close to the surfaces and a coarser gel more distally, consistent with the expected drop in thrombin concentration with distance from the cells on which it is made. Studies of the early stages of fibrin polymerization [1, 4, 5] suggest that much, but not all, of the final gel architecture (branch point density and pore size) is determined by the time of gelation, and that most fiber thickening occurs later.

One of the factors that influences the structure of a fibrin clot is the concentration of thrombin which, as described above, converts molecules of fibrinogen into fibrin monomers, and does so at a rate that depends on the thrombin concentration. Hence the thrombin concentration influences the rate of fibrin monomer supply during fibrin polymerization and gelation. In this paper, we do not explicitly include thrombin, and instead we use variations in the specified rate of supply of fibrin monomers as a surrogate for variations in thrombin concentration. The model we presented in [9] provided a plausible mechanism of fibrin branch formation and showed that it could account for sensitivity of the resulting gel to the rate of monomer supply (i.e., to the concentration of thrombin in the system) as seen

experimentally. Using a small set of ordinary differential equations (ODEs) for moments of the polymer distribution, we studied the behavior of the model up to the time that a gel formed. Gel formation in the model corresponds to a finite time blow-up of a second moment of the oligomer size and structure distribution functions (concentrations). The ODE model in [9] does not hold after a gel forms. In the context of a simpler kinetic model of polymerization (discussed below) studied by Ziff and Stell [26], we provided a framework for extending polymerization studies past gel time [10]. In the current paper, we extend that framework to our fibrin branching model in order to study its behaviors both before and after gel formation occurs. Other kinetic models have been developed to study fibrin polymerization [13, 19, 22], but they do not account for branch formation.

Ziff and Stell [26] studied a kinetic polymerization model with gelation which tracks concentrations c_k of k-mers made from k identical monomers each with f functional units or binding sites. Binding reactions between functional sites on different molecules lead to formation of larger polymers, with the restriction that no loop formation is allowed. In the Ziff–Stell model, gelation is guaranteed to occur for any nonzero initial concentration of monomers only if the number of functional sites per monomer $f > 2$. In our model of fibrin polymerization [9], we track concentrations c_{mb} of clusters with b branches and comprised of $m + 2b$ monomers. The model allows two types of reactions: bimolecular “linking” reactions lead to oligomer elongation and trimolecular “branching” reactions result in new branch formation. Monomers in our model have $f = 2$ functional sites, and so gelation is possible only because of branching reactions which result in clusters with three or more functional sites. As reactions proceed, the average number of functional sites per oligomer, which we refer to as f^A, evolves at a rate determined by the relative numbers of linking and branching reactions that occur. The time required for a gel to form depends on the relative numbers of these two types of reactions, and the resulting gel structure is sensitive to the rate at which monomers are supplied to the system (a surrogate for the thrombin concentration). In [9] we looked only at well-mixed systems from the start of polymerization until a gel formed.

In the current paper, we look also at how polymerization proceeds after the gel has formed. To extend our model [9] beyond the gel time, we must make assumptions about the types of reactions in which the gel can participate. In their analysis, Ziff and Stell [26] considered three distinct post-gelation scenarios in which (i) reactive sites in the gel do not react at all; (ii) reactive sites in the gel react with other reactive sites on the gel as well as those on finite-size oligomers; or (iii) reactive sites on the gel react only with sites on finite-sized oligomers. In this paper, we present results only for the third scenario because only it produces results that agree with those from stochastic simulations involving large numbers of fibrin monomers (also see [10]).

We also investigate the effects of spatial heterogenity and diffusive transport on the evolution of the fibrin gel structure, because conversion of fibrinogen depends on the concentration of thrombin, which itself is likely to be spatially heterogeneous. Because thrombin production is localized to activated platelet surfaces, and, when released into the plasma, can be rapidly inactivated by antithrombin and other inhibitors [7] its concentration is likely to be large only near the activated platelets on which it is produced. Similarly, in some *in vitro*

experiments thrombin is produced by reactions on cellular surfaces and then released [2, 3, 21]. In both situations, conversion of fibrinogen to fibrin is believed to occur predominantly in the neighborhood of the cells on which thrombin is made. These situations therefore correspond to the spatially localized sources of fibrin that we explore in this paper.

2. FIBRIN POLYMERIZATION MODEL.

2.1. Basic Model.

As in [9], we regard a fibrin monomer as a long, linear molecule comprised of two half-monomer domains denoted S (see Fig. 2). The monomer has two kinds of binding sites, those at its ends (depicted by a square) and those in the middle (depicted by a circle), so each half-monomer has one of each type of binding sites. A circle of one molecule can bind to a square of another molecule and this allows for staggered polymerization. Because of the staggering, a linear polymer always has two free ends, each of which consists of the half-monomer S. We refer to such a free end as an active site. Two distinct bonds have to form for linear polymerization, end to middle and middle to end. We do not consider the intermediate state (denoted by Z in Fig. 2a) in which one bond has formed, but instead only the overall process of linear polymerization which we assume occurs at rate $k_l[S]^2$, see Fig. 2a. We call this process “link formation”. Fibrin linear polymerization is a two step process, so the possibility exists that the second step is prevented by binding with other free ends, creating a structure we refer to as a branch (see Fig. 2b). Again we consider only the overall reaction of “branch formation”, which we assume occurs at rate $k_b[S]^3$.

With linear polymerization and branch formation as the only two possible reactions, we examine the formation of clusters. We describe a cluster using two indices, m and b, where b is the number of branch points, and $m + 2b$ is the total number of monomers in the cluster. We denote such a cluster by C_{mb} and its concentration at location $\mathbf{x}$ at time t by $c_{mb}(\mathbf{x}, t)$. With this notation, a single monomer has $m = 1$, $b = 0$, and a simple branch (shown in Fig. 2b) has $m = 1$, $b = 1$.

We allow two types of reactions between clusters. The first is the combination of two clusters to form a new link

$$C_{m_1 b_1} + C_{m_2 b_2} \xrightarrow{k_l} C_{m_1 + m_2,\, b_1 + b_2}, \tag{2.1}$$

and the second is the formation of a new branch point by a trimolecular reaction combining three active sites

$$C_{m_1 b_1} + C_{m_2 b_2} + C_{m_3 b_3} \xrightarrow{k_b} C_{m_1 + m_2 + m_3 - 2,\, b_1 + b_2 + b_3 + 1}\,. \tag{2.2}$$

For mathematical tractability, we also assume that there are no self interactions between the active sites in a single cluster, i.e., no loops, so that the number of active sites in a cluster is $b + 2$.

In [9], we assumed that the dynamics of the cluster concentrations c_{mb}, $m = 1, 2, \ldots$, $b = 0, 1, 2\ldots$, were described by the system of ordinary differential equations

$$\begin{aligned}\frac{dc_{mb}}{dt} &= \frac{k_l}{2}\sum_{\{b_1+b_2=b\}}\sum_{\{m_1+m_2=m\}}(b_1+2)(b_2+2)c_{m_1b_1}c_{m_2b_2}\\ &- k_l(b+2)c_{mb}\sum_{b_1}\sum_{m_1}(b_1+2)c_{m_1b_1}\\ &+ \frac{k_b}{6}\sum_{\{b_1+b_2+b_3=b-1\}}\sum_{\{m_1+m_2+m_3=m+2\}}(b_1+2)(b_2+2)(b_3+2)c_{m_1b_1}c_{m_2b_2}c_{m_3b_3}\\ &- \frac{k_b}{2}(b+2)c_{mb}\sum_{b_1,b_2}\sum_{m_1,m_2}(b_1+2)(b_2+2)c_{m_1b_1}c_{m_2b_2}+S_{mb}\end{aligned} \tag{2.3}$$

.

The first two terms on the right hand side of Eq. 2.3 describe the bimolecular reactions and use reaction rates that are the same as used by Ziff and Stell [26]. The next two terms describe the trimolecular reactions and are based on the same fundamental principle. These rates follow the law of mass action when reacting clusters are all different, but deviate from it when two or more of the reacting clusters are the same. The final term S_{mb} in the equation represents the source of clusters of type m, b. Below, we make the assumption that only S_{10} may be nonzero.

2.2. Up to Gel Time.

In [9], we generalized an idea of Ziff and Stell in introducing a generating function

$$g(t,y,z)=\sum_{m,b}y^m z^{b+2}c_{mb}(t),$$

and used Eqs. 2.3 to derive a single nonlinear partial differential equation for g:

$$g_t=\frac{k_l}{2}(g_z)^2-k_l z g_z R_s+\frac{k_b}{6y^2}(g_z)^3-\frac{k_b}{2}z g_z R_s^2+P, \tag{2.5}$$

where $R_s(t)$ is defined below and $P(t,y,z)=\sum_{m,b}y^m z^{b+2}S_{mb}(t)$. Since we allow only S_{10} to be nonzero, $P(t,y,z)=yz^2S_{10}(t)$. Quantities of interest can be expressed in terms of the distribution of oligomers $\{c_{mb}(t)\}$:

$$R_s=\sum_{m,b}(b+2)c_{mb}, \tag{2.6}$$

$$B_s=\sum_{m,b}bc_{mb},\ \text{and} \tag{2.7}$$

$$\theta_s=\sum_{m,b}(m+2b)c_{mb}\,. \tag{2.8}$$

(In [9], we referred to these as R, B, and M, respectively.) We refer to finite-sized oligomers that are in the solution phase as “sol” and denote sol quantities with subscript “s”. R_s, B_s, and θ_s are the concentration of available reaction sites, the concentration of branches, and

the total concentration of monomers in the sol. Analogous quantities in the gel are denoted with subscript "g". We define the average number of monomers in an oligomer, which we call the average cluster size, as

$$A_s(t) = \frac{1}{\theta_s(t)} \sum_{m,b} (m + 2b)^2 c_{mb}\,. \tag{2.9}$$

Gelation occurs if $A_s(t) \to \infty$ at a finite time t_{gel}. Each of the quantities of interest can be expressed in terms of low-order moments of the oligomer distribution,

$$M_{jk} = \frac{\partial^{j+k} g}{\partial y^j \partial z^k}\bigg|_{y=1,\, z=1}$$

for $j \le 2$ and $k \le 2$. Using Eq. 2.5, we derived ODEs for these moments and from those we derived ODEs for the quantities of interest.

$$\frac{dR_s}{dt} = -k_l R_s^2 - \frac{k_b}{2} R_s^3 + 2S_{10}, \tag{2.10}$$

$$\frac{dB_s}{dt} = \frac{k_b}{6} R_s^3, \tag{2.11}$$

$$\frac{dc_{10}}{dt} = -\left(2k_l R_s + k_b R_s^2\right) c_{10} + S_{10}, \tag{2.12}$$

$$\frac{d\theta_s}{dt} = S_{10}, \tag{2.13}$$

$$\frac{d^2U}{dt^2} = -\frac{k_b}{2} a R_s^3 U + \left(k_b R_s^2 + \frac{a'}{a}\right)\frac{dU}{dt}, \tag{2.14}$$

where $a = k_l + k_b R_s$. The function U has initial values $U(0) = 1$ and $\frac{dU}{dt}(0) = 0$. It was derived from an expression related to A_s by a Riccati transformation [9], (specifically $-\frac{dU}{dt}/(aU) = M_{02} - R$) and provides a convenient indicator of gelation because $U \to 0$ as $t \to t_{gel}$ if and only if $A_s(t) \to \infty$ as $t \to t_{gel}$. The moment $M_{00}(t)$, which gives the total concentration of all molecules, is also of interest because $f^A(t) = R_s(t)/M_{00}(t)$ is the average number of available reaction sites per molecule at time t. M_{00} satisfies the ODE

$$\frac{dM_{00}}{dt} = -\frac{k_l}{2} R_s^2 - \frac{k_b}{3} R_s^3 + S_{10}\,. \tag{2.15}$$

For use in discussing post-gel dynamics, we introduce quantities R, B, and θ, which are the total reactive site concentration, total branch concentration, and total mass density, and we

define $R_g = R - R_s$, $B_g = B - B_s$, and $\theta_g = \theta - \theta_s$. These are the reaction site concentration, branch point concentration, and mass density of the gel. Equations for these quantities are derived below.

In [9], we showed that for any positive initial quantity of monomer $c_{10}(0) > 0$ or any positive constant source of monomer $S_{10} > 0$, $A_s(t) \to \infty$ at a finite time t_{gel} we refer to as the gel time. By solving Eqs. 2.10–2.14, we studied the development of the average oligomer size and branch concentration up to gel time and characterized the dependence of these quantities at that time on the rate of supply of monomer. The gel time itself depends on the size of the initial monomer concentration and/or the rate of monomer supply, as well as on the rate constant k_b. We showed that the branch concentration at t_{gel} is significantly affected by the rate of monomer supply.

To facilitate our discussions below, we use R_s to rewrite Eqs. 2.3 as

$$\begin{aligned}\frac{dc_{mb}}{dt} &= \frac{k_l}{2}\sum_{\{b_1+b_2=b\}}\sum_{\{m_1+m_2=m\}}(b_1+2)(b_2+2)c_{m_1b_1}c_{m_2b_2} - k_l(b+2)c_{mb}R_s \\ &+ \frac{k_b}{6}\sum_{\{b_1+b_2+b_3=b-1\}}\sum_{\{m_1+m_2+m_3=m+2\}}(b_1+2)(b_2+2)(b_3+2)c_{m_1b_1}c_{m_2b_2}c_{m_3b_3} \\ &- \frac{k_b}{2}(b+2)c_{mb}R_s^2 \\ &+ S_{mb},\end{aligned} \tag{2.16}$$

and, for convenience, we repeat the ODE for R_s here,

$$\frac{dR_s}{dt} = -k_l R_s^2 - \frac{k_b}{2}R_s^3 + 2S_{10}\,. \tag{2.17}$$

Eqs. 2.16 and 2.17 form a closed system, but they hold *only* until gel time.

2.3. Beyond Gel Time.

2.3.1. Modified dynamics.—To go beyond t_{gel}, we must postulate the post-gel dynamics. Our assumption in this paper is that gel reactive sites can react with those on finite-sized oligomers but not with other gel reactive sites as in the third scenario considered by Ziff and Stell [26]. This is consistent with the assumption underlying Eqs. 2.16 that formation of cycles is not permitted. To implement this assumption, we first modify Eqs. 2.16–2.17 by replacing each occurence of R_s by the total concentration of reactive sites R. Then, we subtract terms that describe interactions involving two or more reaction sites on the gel. Since $R = R_s + R_g$, we note that $R^2 = R_s^2 + 2R_sR_g + R_g^2$ and $R^3 = R_s^3 + 3R_s^2R_g + 3R_sR_g^2 + R_g^3$. The expressions R_g^2 and R_g^3 arise from reactions between pairs or triplets of gel reactive sites, respectively, and so we remove them from the equations. Specifically, we modify Eq. 2.16 by replacing R_s by R in the second term and by replacing R_s^2 by $R^2 - R_g^2$ in the fourth term on the right hand side. We modify Eq. 2.17 by replacing R_s^2 by $R^2 - R_g^2$ and R_s^3 by $R^3 - \left(3R_sR_g^2 + R_g^3\right)$.

We also extend the model by allowing oligomer and gel concentrations to vary in space (**x**), and finite-sized oligomers, but not gel, to move. In this paper we consider only diffusive movement, but it is straightforward to also include advective motion of oligomers as we did in [25]. Taking into account our assumptions about post-gelation reactions and diffusive movement of oligomers, the equations for $c_{mb}(\mathbf{x}, t)$ and $R(\mathbf{x}, t)$ are the infinite set of partial differential equations

$$\begin{aligned}(c_{mb})_t &= \nabla \cdot (D \nabla c_{mb}) \\ &+ \frac{k_l}{2} \sum_{\{b_1 + b_2 = b\}} \sum_{\{m_1 + m_2 = m\}} (b_1 + 2)(b_2 + 2) c_{m_1 b_1} c_{m_2 b_2} - k_l (b + 2) c_{mb} R \\ &+ \frac{k_b}{6} \sum_{\{b_1 + b_2 + b_3 = b - 1\}} \sum_{\{m_1 + m_2 + m_3 = m + 2\}} (b_1 + 2)(b_2 + 2)(b_3 + 2) c_{m_1 b_1} c_{m_2 b_2} c_{m_3 b_3} \\ &- \frac{k_b}{2} (b + 2) c_{mb} \left(R^2 - R_g^2 \right) \\ &+ S_{10} \delta_{m1} \delta_{b0},\end{aligned} \tag{2.18}$$

and

$$\begin{aligned}R_t &= \nabla \cdot (D \nabla R_s) \\ &- k_l \left(R^2 - R_g^2 \right) - \frac{k_b}{2} \left(R^3 - \left(3 R_s R_g^2 + R_g^3 \right) \right) + 2 S_{10}\end{aligned} \tag{2.19}$$

and we assume that they hold for all $t \geq 0$ and for **x** in a specified domain with boundary conditions discussed below. Until the time a gel forms, $R = R_s$ and $R_g = 0$, and these equations represent a spatial extension of Eqs. 2.16–2.17. After a gel forms, $R_s(\mathbf{x}, t) = \sum_{m,\, b} (b + 2) c_{mb}$ and $R_g(\mathbf{x}, t) = R(\mathbf{x}, t) - R_s(\mathbf{x}, t)$.

2.3.2. Reformulation using generating function.—To study Eqs. 2.18–2.19 before and after gel time, we again introduce a generating function

$$g(\mathbf{x}, t, y, z) = \sum_{m,\, b} y^m z^{b+2} c_{mb}(\mathbf{x}, t), \tag{2.20}$$

and find that

$$\begin{aligned}g_t &= \nabla \cdot (D \nabla g) \\ &+ \frac{k_l}{2} (g_z)^2 - k_l z g_z R + \frac{k_b}{6 y^2} (g_z)^3 - \frac{k_b}{2} z g_z \left(R^2 - R_g^2 \right) + y z^2 S_{10}\,.\end{aligned} \tag{2.21}$$

In these equations, z and y are "dummy" variables from the generating function, they do not refer to the spatial coordinates which are denoted **x**. In the derivation of Eq. 2.21, we made use of the assumptions that all oligomers have the same diffusion coefficient D. It is not possible, in general, to reduce equations 2.18 to a single PDE for g if the oligomer diffusivities depend on the oligomer size and structure, *i.e.*, if D is replaced by D_{mb} in 2.18. However, it is straightforward to allow a finite-number of oligomer species to have larger diffusion coefficients than other oligomers. If this is done for monomers only, then we must solve a separate PDE for the monomer concentration as well as make a small modification

to the equation for g above. For details, see Supplement section S1.2 and [10]. Further discussion of our assumptions in modeling oligomer diffusion is given in Section 4.

Following its successful use by Ziff and Stell [26], we make the change of variables

$$\widetilde{W}(\mathbf{x}, t, y, z) = zR(\mathbf{x}, t) - g_z(\mathbf{x}, t, y, z)\,. \tag{2.22}$$

It follows from the PDEs for g and R that $\widetilde{W}$ satisfies the equation

$$\begin{aligned}\widetilde{W}_t = {} & \nabla\cdot\left(D\nabla\left(\widetilde{W} - z\widetilde{W}\big|_{y=z=1}\right)\right)\\ & - \left\{\frac{k_l}{2}\widetilde{W}^2 + \frac{k_b}{6y^2}(zR-\widetilde{W})^3 - \frac{k_b}{2}\left(R^2 - R_g^2\right)\left(z^2R - z\widetilde{W}\right)\right\}_z\\ & + k_l z R_g^2 - \frac{k_b}{2}z\left(R^3 - \left(3R_sR_g^2 + R_g^3\right)\right) - 2S_{10}z(y-1)\,.\end{aligned} \tag{2.23}$$

This equation describes diffusion of a quantity related to $\widetilde{W}$ with respect to the spatial variable $\mathbf{x}$ and "transport" of $\widetilde{W}$ in the variable z with flux function $\frac{k_l}{2}\widetilde{W}^2 + \frac{k_b}{6y^2}(zR-\widetilde{W})^3 - \frac{k_b}{2}\left(R^2 - R_g^2\right)\left(z^2R - z\widetilde{W}\right)$. Because of the presence of $\widetilde{W}(x,t,1,1)$ in the diffusion term, the equation for $\widetilde{W}$ is *nonlocal* in the variable z.

As we show below, to calculate the quantities of interest to us requires $W(\mathbf{x},t,z) \equiv \widetilde{W}(\mathbf{x},t,y=1,z)$ and $V(\mathbf{x},t,z) \equiv \widetilde{W}_y(\mathbf{x},t,y=1,z)$. To obtain an evolution equation for W, we simply set $y = 1$ in Eq. 2.23. To obtain an evolution equation for V, we use Eq. 2.23 to derive a PDE for $\widetilde{W}_y$ and then set $y = 1$ in that PDE. The resulting equations are

$$\begin{aligned}W_t = {} & \nabla\cdot\left(D\nabla\left(W - zW\big|_{z=1}\right)\right)\\ & - \left\{\frac{k_l}{2}W^2 + \frac{k_b}{6}(zR-W)^3 - \frac{k_b}{2}\left(R^2 - R_g^2\right)\left(z^2R - zW\right)\right\}_z\\ & + k_l z R_g^2 - \frac{k_b}{2}z\left(R^3 - \left(3R_sR_g^2 + R_g^3\right)\right),\end{aligned} \tag{2.24}$$

$$\begin{aligned}V_t = {} & \nabla\cdot(D\nabla V) - \left\{\left(k_lW - \frac{k_b}{2}(zR-W)^2 + \frac{k_b}{2}z\left(R^2 - R_g^2\right)\right)V\right\}_z\\ & + k_b\left((zR-W)^2(R-W_z)\right) - 2S_{10}z\,.\end{aligned} \tag{2.25}$$

The concentration of reactive sites in the gel, $R_g(\mathbf{x}, t)$, can be obtained from W, in fact,

$$R_g(\mathbf{x}, t) = W(\mathbf{x}, t, 1)\,. \tag{2.26}$$

To see this, note that $R_g = R - R_s$, $R_s = \sum_{m,b}(b+2)c_{mb}$, and $W|_{z=1} = R - g_z|_{y=1,z=1} = R - R_s$. Hence, using Eq. 2.26, we see that Eqs. 2.19 and 2.24–2.25 form a closed system. Values of V are used to calculate quantities of interest (see below) but do not affect the dynamics of W and R.

2.3.3. Other Physical Quantities.—Recall that the sol mass density, branch concentration, reactive site concentration, and total concentration of oligomers are $\theta_s(\mathbf{x},t)=\sum_{m,b}(m+2b)c_{mb}$, $B_s(\mathbf{x},t)=\sum_{m,b}bc_{mb}$, $R_s(\mathbf{x},t)=\sum_{m,b}(b+2)c_{mb}$, and $M_{00}(\mathbf{x},t)=\sum_{m,b}c_{mb}$, respectively. These can be expressed in terms of $W(\mathbf{x},t,z)$ and $V(\mathbf{x},t,z)$:

$$\theta_s(\mathbf{x},t)=4\int_0^1 W(\mathbf{x},t,z')dz'-\int_0^1 V(\mathbf{x},t,z')dz'-2W(\mathbf{x},t,1), \tag{2.27}$$

$$B_s(\mathbf{x},t)=2\int_0^1 W(\mathbf{x},t,z')dz'-W(\mathbf{x},t,1), \tag{2.28}$$

$$R_s=R-R_g=R-W|_{z=1}, \tag{2.29}$$

and

$$M_{00}=\frac{1}{2}(R_s-B_s). \tag{2.30}$$

The first three of these relations are derived in Supplement section S1.1, and the fourth follows immediately from the definitions of the quantities involved. θ_g and B_g can be computed from Eqs. 2.27–2.29 and the total mass density θ and branch concentration B as $\theta_g(\mathbf{x},t)=\theta(\mathbf{x},t)-\theta_s(\mathbf{x},t)$ and $B_g(\mathbf{x},t)=B(\mathbf{x},t)-B_s(\mathbf{x},t)$ provided we know θ and B. To determine them, we solve the PDEs

$$\theta_t=\nabla\cdot(D\nabla\theta_s)+S_{10}, \tag{2.31}$$

$$B_t=\nabla\cdot(D\nabla B_s)+\frac{k_b}{6}\left(R^3-\left(3R_sR_g^2+R_g^3\right)\right). \tag{2.32}$$

Eq. 2.31 follows from the facts that in the domain interior, mass is produced only through the supply of monomers, and that the mass can be redistributed in space by diffusion of finite-size clusters. The rate of branch production in Eq. 2.32 is one third of the rate of disappearance of reactive sites when branches form (see Eq. 2.19) because three reactive sites disappear whenever a branch is formed. Like mass, branches can be redistributed in space by the diffusion of branches on finite-sized clusters.

2.3.4. Boundary Conditions.—When we consider the PDE model, Eqs. 2.19, 2.24–2.29, and 2.31–2.32, in a bounded region Ω, we require boundary conditions. We restrict ourselves to situations in which monomer is produced at the rate $F_{10}(\mathbf{x},t)$ at a point $\mathbf{x}\in\partial\Omega$. The boundary conditions for c_{mb} are

$$-D\mathbf{n}\cdot\nabla c_{mb}(\mathbf{x},t)=F_{10}(\mathbf{x},t)\delta_{m1}\delta_{b0}, \tag{2.33}$$

where **n** is the unit normal pointing into Ω at **x**. In Supplement section S1.4, we use Eq. 2.33 to derive boundary conditions for R, W, V, θ_s, and B_s, valid for any $F_{10}(\mathbf{x}, t)$, but in the results of this paper, we consider only $F_{10}(\mathbf{x}, t) = 0$, and give the corresponding boundary conditions here.

$$-D\mathbf{n}\cdot\nabla R(\mathbf{x},t) = -D\mathbf{n}\cdot\nabla R_g, \tag{2.34}$$

$$-D\mathbf{n}\cdot\nabla W(\mathbf{x},t,z) = -D\mathbf{n}\cdot\nabla R_g(\mathbf{x},t) \text{ and } -D\mathbf{n}\cdot\nabla V(\mathbf{x},t,z) = 0, \tag{2.35}$$

$$-D\mathbf{n}\cdot\nabla\theta_s(\mathbf{x},t) = 0), \text{ and } -D\mathbf{n}\cdot\nabla B_s(\mathbf{x},t) = 0. \tag{2.36}$$

In this paper, we consider the one dimensional domain $\Omega = -L \le x \le L$, assume that D is constant, and we set $F_{10}(-L) = F_{10}(L) = 0$. To determine the monomer distribution c_{10}, we also solve the $m = 1$, $b = 0$ instance of Eqs. 2.18 and 2.33.

3. RESULTS.

In this section we consider a series of computational "experiments" in which we solve the equations of the model under various conditions to explore its behavior. As in [9], we nondimensionalize our variables by scaling all concentrations using a typical concentration C_0, scaling time by $(C_0 k_l)^{-1}$, and defining nondimensional monomer supply rate and branching rate as $S_{10}/\left(k_l C_0^2\right)$ and $k_b C_0/k_l$, respectively. We use the numerical method sketched in section S1.5 in the Supplement and described in more detail in [10] except when we solve the moment equations Eq. 2.10–2.14, in which case we use Matlab's ode23 ODE solver.

3.1. Spatially-uniform initial monomer distribution.

Consider a spatially-uniform initial monomer concentration $c_{10}(0) = m_0^i$ with no source or boundary flux. In this example, we omit reference to the spatial variable x. The corresponding initial conditions are $W(0, z) = 0$, $R(0) = R_s(0) = 2m_0^i$, $V(0, z) = -2m_0^i z$, $\theta(0) = \theta_s(0) = m_0^i$ and $B(0) = B_s(0) = 0$. Fig. 3a shows curves of W as a function of $z \in [0, 1)$ at several times before and after gelation, in red and blue respectively. Before gel time, the curves steepen towards $z = 1$ as time progresses. Gelation occurs when $W_z(t, 1^-) \to -\infty$. After that time, $W(t, 1) > 0$ and, in this simulation, $W(t, 1) = R_g(t)$ continues to grow with time (Fig. 3b) until no finite size oligomers remain (not shown). Fig. 3cd show the time dependence of quantities (c_{10}, R_s, θ_s, and B_s) associated with finite-size oligomers and quantities (R_g, B_g, and θ_g) associated with gel. Early in the simulation, monomers combine to produce oligomers, which combine with other oligomers or monomers to produce larger oligomers, so c_{10} steadily decreases and $\theta_s - c_{10}$ grows. Reactive sites are "consumed" during each interaction, so R_s decreases. Some of the interactions result in branch formation and B_s increases. Beginning at t_{gel}, θ_s and B_s suddenly start to decrease and R_s decreases at a faster rate than earlier, as sol mass, branches, and reactive sites become incorporated into the growing gel. The solution curves in Fig. 3c match those of the ODE system Eqs.

2.10–2.14, studied in [9], up to t_{gel}, but it is not possible to solve Eqs. 2.10–2.14 past t_{gel} when R_g, θ_g, and B_g start to grow from zero, and kinks appear in θ_s, B_s, and R_s. Note that $B_g(t) = R_g(t)$ for all t, as shown in Supplement section S1.3.

3.2. Spatially-uniform constant rate monomer source.

Next, we assume that there is no monomer initially and that monomer is supplied uniformly in space at a constant rate S_{10}. The results shown in Fig. 4 up to t_{gel}, match those shown in Fig. 4 of [9], which were obtained by solving the system Eqs. 2.10–2.14.

To assess our assumptions about post-gelation reactions, we performed stochastic simulations of the reactions in Eqs. 2.1–2.2 in a volume v with no monomers initially and with monomers introduced at a constant average rate of $S_{10}v$. Oligomers $C_{m_1b_1}$ and $C_{m_2b_2}$ form a link during an infinitesimal time interval dt with probability $\frac{k_l}{v}(b_1+2)(b_2+2)n_{m_1b_1}n_{m_2b_2}dt$ if (m_1, b_1) is different from (m_2, b_2), where n_{mb} is the number of oligomers of type C_{mb}. If (m_1, b_1) and (m_2, b_2) are the same, the probability is $\frac{k_l}{2v}(b_1+2)^2 n_{m_1b_1}\left(n_{m_1b_1}-1\right)dt$. Oligomers $C_{m_1b_1}$, $C_{m_2b_2}$, and $C_{m_3b_3}$ form a branch with probability $\frac{k_b}{v^2}(b_1+2)(b_2+2)(b_3+2)n_{m_1b_1}n_{m_2b_2}n_{m_3b_3}dt$ if (m_1, b_1), (m_2, b_2) and (m_3, b_3) are distinct, with probability $\frac{k_b}{2v^2}(b_1+2)^2(b_3+2)n_{m_1b_1}\left(n_{m_1b_1}-1\right)n_{m_3b_3}dt$ if (m_1, b_1) is the same as (m_2, b_2), but different from (m_3, b_3), and with probability $\frac{k_b}{6v^2}(b_1+2)^3 n_{m_1b_1}\left(n_{m_1b_1}-1\right)\left(n_{m_1b_1}-2\right)dt$ if (m_1, b_1), (m_2, b_2), and (m_3, b_3) are the same. The larger the volume v, the more monomers the source introduces before substantial linking or branching reactions occur.

We implemented the simulation using the Gillespie alogorithm [12]. In the stochastic simulations, the average oligomer size cannot "blow up" because there are only a finite number of monomers in total. However, the average oligomer size $A = \left(\sum_{m,b}(m+2b)^2 n_{mb}\right)/\left(\sum_{m,b}(m+2b)n_{mb}\right)$ and the size of the largest oligomer both begin to rise sharply starting at the gel time predicted by the deterministic PDE system, as shown in Fig. 5ab. Fig. 5c shows plots of R, B, θ, and c_{10} from the Gillespie (solid color curves) and PDE model (dashed black curves) simulations based on the assumption that gel reaction sites can bind with those on finite-sized oligomers, but not with other reaction sites on the gel. We see excellent agreement, which is similar to the behavior we saw with the Ziff–Stell gelation model [10]. To further compare dynamics after gelation, we partitioned each of R, B, and θ from the stochastic simulation into a part, denoted R_g, B_g, and θ_g, respectively, corresponding to the largest oligomer and a part corresponding to all of the smaller oligomers. Fig. 5d shows excellent agreement between these R_g, B_g and θ_g as well as B_s and $\theta_s - c_{10}$ and the corresponding PDE model variables from the simulation shown in Fig. 4. This suggests that regarding the gel in the PDE model as approximating the largest oligomer in a large finite system is reasonable.

This is support for the particular choice we made for post-gel kinetics as described in section 2.3.1.

3.3. Spatially-uniform time-varying monomer source.

In these simulations, the spatially-uniform, time-varying source of monomer is given by

$$S_{10}(t) = m_0 \lambda \exp(-\lambda t). \tag{3.1}$$

This source is motivated by experiments in which fibrinogen and thrombin are put in solution at specified concentrations [20], and thrombin proteolytically converts fibrinogen to fibrin. The source term corresponds to that from conversion of fibrinogen to fibrin according to the linearized Michaelis–Menten equation

$$\frac{dG(t)}{dt} = -\frac{k_{\text{cat}} E}{K_M} G(t) \text{ and } S_{10}(t) = \frac{k_{\text{cat}} E}{K_M} G(t), \tag{3.2}$$

where $G(t)$ is the fibrinogen concentration, $G(0) = m_0$ is its initial value, E is the thrombin concentration, and k_{cat} and K_M are the catalytic rate constant and Michaelis–Menten constant for thrombin's conversion of fibrinogen to fibrin. Setting $\lambda = k_{\text{cat}} E / K_M$ gives the formula in Eq. 3.1.

We report on simulations run for a range of m_0, λ, and k_b values. Each simulation is run to a time t_{final} by which 99% percent of the supplied monomer has been incorporated into the gel. Fig. 6 shows how t_{gel} varies with the changes in m_0, λ, and k_b. For each m_0 value, t_{gel} is smallest when both λ and k_b are large, and for fixed (λ, k_b), t_{gel} decreases with increasing m_0. The observed gel times span up to 5 orders of magnitude moving from the lower left to upper right of a heatmap.

For the same simulations, Fig. 7abc show parametric plots of the branch point density at the final time $B_g(t_{final})$ versus that at gel time $B_s(t_{gel})$, as λ and k_b are varied for a fixed value of m_0 (the lowest point on each curve corresponds to the smallest k_b). Several features of these plots noteworthy. For each m_0, $B_s(t_{gel})$ is monotone increasing in λ, but non-monotone in k_b, while $B_g(t_{final})$ is monotone increasing in both λ and k_b. For given m_0 and λ values, two different k_b values can yield very similar values of $B_s(t_{gel})$ and very different values of $B_g(t_{final})$. In many cases, one of these $B_g(t_{final})$ values is only a little greater and the other is much greater than $B_s(t_{gel})$. The heatmaps of the ratio $B_s(t_{gel})/B_g(t_{final})$ in Fig. 7def show this more clearly. For each m_0, there is a range of λ and k_b values for which $B_s(t_{gel})$ is at least 80% of $B_g(t_{final})$, in agreement with recent experimental results [4, 5]. These λ and k_b values seem to satisfy a condition $\log_2 k_b / \log_2 \lambda \leq f(m_0)$, where $f(m_0)$ decreases with m_0. Hence, our model can capture this important experimental observation, but only in certain parameter value ranges.

The curves in Fig. 8 show how t_{gel} and $B_s(t_{gel})$ vary with k_b, for five values of λ. Unsurprisingly, t_{gel} decreases and $B_s(t_{gel})$ increases as λ increases. The gel time also decreases as k_b increases (moving from right to left along each curve), but strikingly, there is a peak in $B_s(t_{gel})$ for an intermediate value of k_b close to 1 for each λ and m_0 value. In Fig. 9 we look at time course data to understand how these behaviors arise.

Fig. 9 shows results up to t_{gel} from the ODE model (Eqs. 2.10–2.14) for simulations run with the three sets of parameters ($m_0 = 4$, $\lambda = 16$, and $k_b = 32$, 1, or 1/8) which produced the leftmost, peak, and rightmost points on the cyan curve in Fig. 8b. Fig. 8b shows that $B_s(t_{gel})$ is approximately the same for $k_b = 32$ and $k_b = 1/8$, and that the peak value of $B_s(t_{gel})$ at $k_b \approx 1$ is approximately twice that at the k_b values at the endpoints of the curves. Fig. 9adg show the different time courses of R_s, B_s, θ_s, and c_{10} for the three k_b values. To understand them, we look in more detail at how links and branches are formed in these simulations. The overall link formation rate can be broken down as

$$\frac{k_l}{2}R_s^2 = 2k_l c_{10}^2 + 2k_l(R_s - 2c_{10})c_{10} + \frac{k_l}{2}(R_s - 2c_{10})^2, \tag{3.3}$$

into the rates at which links form through interactions involving 2, 1, or 0 monomers (i.e., only oligomers), respectively. The overall branch formation rate can be split as

$$\frac{k_b}{6}R_s^3 = \frac{4}{3}k_b c_{10}^3 + 2k_b c_{10}^2(R_s - 2c_{10}) + k_b c_{10}(R_s - 2c_{10})^2 + k_b(R_s - 2c_{10})^3, \tag{3.4}$$

into the rates of branch formation through reactions involving 3, 2, 1, or 0 monomers. These rates are plotted in Fig. 9beh. In Fig. 9cfi, we show the average functionality $f^A(t) = R_s(t)/M_{00}(t)$ plotted as a function of the total mass density of monomer $\theta_s(t)$ that has been injected by time t. Recall that in the Ziff–Stell model, each monomer has f functional reactive sites and that it is necessary that $f > 2$ in order for a gel to form. In our model, $f^A = 2$ for monomers and, thus, $f^A(t)$ depends on the extent of branch formation prior to time t. The concentration and reaction rate curves in Fig. 9 for the different values of k_b are strikingly different.

Fig. 9abc show that with $k_b = 32$, the total monomer concentration θ_s increases throughout the simulation, and it closely tracks the concentration of monomers, c_{10}, up to a time at which $B_s(t)$ noticeably rises. $B_s(t)$ then increases at an accelerating rate until t_{gel}. The branching reaction rates far exceed those for the linking reactions, and branch formation is dominated by reactions involving 2 or 3 monomers. $\theta_s(t_{gel}) \approx 1.5$ compared to the maximum $m_0 = 4$ that the source can inject. f^A increases monotonically from 2 to ≈ 2.68.

Fig. 9def show results with $k_b = 1$. The curves for θ_s and c_{10} first diverge and B_s first noticeably rises at a later time than for $k_b = 32$. B_s continues to increase until t_{gel} while R_s begins to decline about mid-way to t_{gel} in concert with the decreasing rate of monomer supply. The link and branch formation rates are similar; most early reactions involve only monomers. As time progresses, the rates of reactions involving one oligomer increase, followed later by the rates of reactions involving multiple oligomers. While some types of branching reactions slow later in the simulation, others accelerate, and $B_s(t)$ is approximately linear for much of the simulation. Here, t_{gel} is more than 4-fold greater than with $k_b = 32$. By t_{gel}, θ_s reaches $\approx 88\%$ of its possible maximum m_0. f^A increases monotonically from 2 to ≈ 2.75. It remains close to 2 longer than for $k_b = 32$ because linking reactions involving only unbranched oligomers cannot cause f^A to increase.

Fig. 9ghi show that with $k_b = 1/8$, a gel forms substantially later than for $k_b = 1$ or 32. Almost all of the potential monomer source has been injected by $t = 0.29$. At this time, R_s and c_{10} are decreasing quickly and B_s is increasing slowly. Much of the branch formation occurs after monomer injection is essentially complete, and so draws on a rapidly decreasing pool of monomers and small oligomers. Link formation outpaces branch formation and primarily comprises reactions involving 2 monomers. Early branch formation primarily involves 2 or 3 monomers, but after the source is exhausted, branch formation by 3 oligomers dominates. Because linking reactions involving 2 monomers predominate for much of the simulation, f^A increases very slowly during the first half of the simulation; it increases from below 2.2 to over 2.9 after monomer injection is essentially complete.

$B_s(t_{gel})$ is also not monotonic in k_b for constant source rates. Because these observations pertain to $t < t_{gel}$, we can use Eqs. 2.10–2.14, with a constant source S_{10}, to investigate the origin of the intriguing non-monotonicities shown in Fig. 8. The colored curves in Fig. 10a show $B_s(t_{gel})$ for such simulations for a large range of S_{10} and k_b values. For each S_{10}, there is a well-defined peak for an intermediate value of k_b. It occurs at $k_b = O(1)$, $k_b \ll 1$ and $k_b \gg 1$ for intermediate, large, and small values of S_{10}, respectively. $B_s(t_{gel})$ scales like $k_b^{1/2}$ for small k_b and like $k_b^{-1/3}$ for large k_b. The peak occurs during the transition between these two behaviors.

To understand the origin of these scaling behaviors, suppose that R_s is in quasisteady state, so that from Eq. 2.10, $R_s = r_{ss}$ where r_{ss} satisfies

$$0 = -k_l r_{ss}^2 - \frac{k_b}{2} r_{ss}^3 + 2S_{10}. \tag{3.5}$$

Then, Eq. 2.14 simplifies to the constant-coefficient linear equation

$$U'' - \left(k_b r_{ss}^2\right)U' + \frac{k_b}{2}(k_l + k_b r_{ss}) r_{ss}^3 U = 0. \tag{3.6}$$

The solution to this equation which satisfies $U(0) = 1$ and $U'(0) = 0$ is

$$U(t) = e^{\frac{k_b r_{ss}^2}{2} t}\left[\cos\left(\frac{\Delta}{2}t\right) - \frac{k_b r_{ss}^2}{\Delta}\sin\left(\frac{k\Delta}{2}t\right)\right], \tag{3.7}$$

where $\Delta \equiv r_{ss}\sqrt{2k_l k_b r_{ss} + k_b^2 r_{ss}^2}$. Since, $U(t_{gel}) = 0$, we find that

$$t_{gel} = \frac{2}{\Delta}\arctan\left(\frac{\Delta}{k_b r_{ss}^2}\right), \tag{3.8}$$

under the assumption that $R_s(t) \equiv r_{ss}$. From Eq. 2.11, with $R_s = r_{ss}$ constant, we see that

$$B_s\left(t_{gel}\right) = \frac{k_b}{6} r_{ss}^3 t_{gel} = \frac{r_{ss}}{3\sqrt{1 + \frac{2k_l}{k_b r_{ss}}}}\arctan\left(\sqrt{1 + \frac{2k_l}{k_b r_{ss}}}\right). \tag{3.9}$$

When $k_b \gg 1$, S_{10} is at least of moderate size, and we assume that the terms $\frac{k_b}{2}R_s^3$ and $2S_{10}$ in Eq. 3.5 balance, $r_{ss} \approx \left(\frac{4S_{10}}{k_b}\right)^{1/3}$ and $t_{gel} \approx \frac{\pi}{2k_b r_{ss}^2}$. When $k_b \ll 1$ and we assume that the terms $k_l R_s^2$ and $2S_{10}$ balance, $r_{ss} \approx (2S_{10}/k_l)^{1/2}$ and $t_{gel} \approx \frac{\pi}{r_{ss}\sqrt{2k_b r_{ss}}}$. Using the limiting expressions for r_{ss} in Eq. 3.9, we find that

$$B_s(t_{gel}) \approx \begin{cases} \frac{\pi r_{ss}}{12} = O\left(k_b^{-1/3}\right) & \text{if } k_b \gg 1 \\ \frac{\pi r_{ss}^{3/2}}{6\sqrt{2}} k_b^{1/2} = O\left(k_b^{1/2}\right) & \text{if } k_b \ll 1. \end{cases} \tag{3.10}$$

Substituting the numerical solution of Eq. 3.5 into Eq. 3.10 yields the black curves in Fig. 10a, which are in excellent agreement with the corresponding colored curves.

In the examples in Fig. 9, average functionality $f^A(t_{gel})$ increases monotonically in t from 2 at $t = 0$ towards a value between 2.6 and 3 at t_{gel}. In Fig. 10b, we see that, for a wide range of S_{10}, $f^A(t_{gel})$ approaches 2 from above as k_b approaches 0, and it approaches a value close to 2.7 as k_b becomes very large. The transition between these behaviors shifts leftward as S_{10} increases. To understand the asymptotic results, we first note that the relation $R_s = B_s + 2M_{00}$ implies that

$$f^A = \frac{R_s}{M_{00}} = \frac{2}{1 - \frac{B_s}{R_s}}. \tag{3.11}$$

Then, using the asymptotic values of $B_s(t_{gel})$ and r_{ss} from Eq. 3.10 and the text above it, respectively, we find that for $k_b \ll 1$, $\frac{B_s(t_{gel})}{R_s(t_{gel})} = O\left(\sqrt{\frac{k_b}{2S_{10}}}\right)$ and therefore $f^A(t_{gel}) \to 2^+$ as $k_b \to 0$. For $k_b \gg 1$, Eq. 3.10 implies that $\frac{B_s(t_{gel})}{R_s(t_{gel})} \to \frac{\pi}{12}$ and so $f^A(t_{gel}) \to 2/\left(1 - \frac{\pi}{12}\right) = 2.7093$, which is the height of the dashed blue horizontal line in Fig. 10b. The origin of the gap between the dashed blue line and the colored curves is explored in Supplement section S1.6. Fig. 10c shows plots of $f^A(t_{gel})$ for the source $S_{10}(t) = m_0\lambda \exp(-\lambda t)$ with $m_0 = 4$ and $\lambda \in [10^{-5}, 10^5]$. For each λ, f^A seems to approach the same limit as for the constant source case for $k_b \to \infty$, while for $k_b \to 0$, it asymptotes to 3. As shown in Supplement section S1.7, $f^A \to 3$ as $t \to t_{gel}$ for any positive branching rate k_b when starting with an initial supply of monomer and 0 source. Here, with $k_b \ll 1$, the source is essentially depleted after a time of order λ^{-1} that is much shorter than the branch formation time scale k_b^{-1}. Therefore, the system behaves much like one with an initial supply of monomer.

3.4. Temporally and spatially varying monomer source.

We next look at the PDE system's behavior before and after gelation when there is no monomer initially and monomer is supplied at the temporally and spatially varying rate

$$S_{10}(x,t) = m_0 \lambda \exp(-\lambda t) s(x), \tag{3.12}$$

where $s(x) = 1 + \cos(\pi \cdot x/h)$ for $|x| < h = 0.1$ and $s(x) = 0$ otherwise. In the following sections we look at the effects of variations in the source rate λ, branching rate k_b, and diffusion coefficient D.

3.4.1. Variations in Source Rate λ.—We begin with $m_0 = 8$, $k_b = 4$, and $\lambda = 1/4$, 1, or 4, so the rate, but not the amount of monomer supplied varies. Fig. 11a shows the contour $R_g(x, t) = 0.001$ for each λ. Since $R_g(x, t)$ first becomes nonzero when a gel forms at location x, these contours show the propagation of the gel front toward the domain boundary. The front propagates quickly across the support of the source, slows for intermediate values of x, and speeds up when approaching the no-flux boundary at $x = 0.5$. Gel formation within the source's support occurs sooner for larger λ, but the gel front for $\lambda = 1$ "catches" that for $\lambda = 4$ about midway across the domain and reaches the boundary sooner.

Fig. 11bcd show contours of $R_g(x, t)$ for λ =1/4, 1, and 4. For $\lambda = 1/4$, the lowest value contours rapidly cross the domain, and there is a long delay between the start of gelation at $x = 0$ and $R_g(0, t)$ reaching 0.5. For $\lambda = 1$, this delay is much shorter, while propagation of higher values of R_g toward the domain boundary is slower. For $\lambda = 4$, there is very little delay between the onset of gelation at $x = 0$ and $R_g(0, t)$ reaching 0.5. In contrast, R_g grows much more slowly than for the smaller λ values at locations midway between the source and the boundary. For $\lambda = 4$, R_g reaches 0.005 at $x = 0.5$ much earlier than it does at $x = 0.35$. These observations reflect the relative extent to which monomers introduced in the source region become part of the gel there as opposed to diffusing toward the boundary. With $\lambda = 4$, the rapidly cascading growth of oligomers near $x = 0$ "absorbs" much of the monomer before it can diffuse away. For $\lambda = 1/4$, diffusion keeps up with the introduction of monomer, and the gel develops more slowly at $x = 0$ and faster at locations near the boundary.

For $\lambda = 1$, Fig. 12 shows snapshots of the spatial evolution of the sol and gel variables and of two derived indicators of oligomer and gel structure: the structure parameter, $B(x, t)/\theta(x, t)$, which is the ratio of the total branch point density in both the sol and gel to the total mass density, and the average functionality $f^A(x, t) = R_s(x, t)/M_{00}(x, t)$. Fig. 12 shows the base case to which other results, presented in the Supplement, should be compared. Recall that $f^A(x, t) > 2$ is required for gelation to occur, and that monomers in our model have functionality 2. The first four rows show the situation at times by which 18, 39, 63, and 86% of the monomer has been delivered by the source. At the earliest times, the peak sol densities occur at $x = 0$. At $t = 0.2$, θ_s is only moderately larger than c_{10} at $x = 0$ indicating that most molecules there are monomers. At the boundary $x = 0.5$, $c_{10} \approx \theta_s > 0$, signifying that monomer has reached the domain boundary but that few larger oligomers are present there. $f^A(0, t)$ has increased somewhat from its base value 2. By $t = 0.5$, θ_s and B_s at $x = 0$ have grown significantly, while c_{10} is lower there despite the continued activity of the source. $f^A \approx 2.4$ within the source region and is above 2 throughout the rest of the domain.

By $t = 1.0$, gel covers the source region, but is most prominent near $x = 0$. Values of θ_s, B_s, and c_{10} are lower there than earlier because finite-size oligomers have been incorporated into the gel. Gel has formed throughout the domain, but $\theta_g(0.5, 1)$ is $5 \cdot 10^4$-fold smaller than $\theta_g(0, 1)$. f^A is lower within the source's support and higher for $|x| > 0.25$. B/θ is significantly higher near $x = 0$ than outside of the source region. The trends continue through $t = 5$, with θ_g and B_g increasing mainly within the source region. f^A drops back towards 2 throughout the domain, as multi-branched oligomers are incorporated into the gel, while B/θ is relatively high over a much broader region. So much finite-sized oligomer within the source region becomes part of the gel that a "reverse" diffusive gradient in θ_s develops, particularly for intermediate $|x|$, and finite-size oligomers diffuse from this region *toward* $x = 0$. Between $t = 5$ and $t = 10$, θ_g increases a little throughout the domain and at $t = 10$, over 98% of the total sourced monomer is in the gel. B/θ is higher throughout the domain than earlier and f^A is now uniformly ≈ 2.1.

Supplement Fig. S2 shows similar snapshots for the slower source rate $\lambda = 1/4$. The salient differences from the $\lambda = 1$ results are that oligomer and branch formation, and the onset of gelation are slower within the source region. Sol variables are more homogeneous in space as are gel variables later in the simulation. At $t = 10$, most branches are in the gel and so $f^A \approx 2$ for all x. No reverse gradient in sol concentrations is present, so sol species continue to diffuse toward the boundaries. At $x = 0.5$, θ_g reaches a value almost three times that for $\lambda = 1$. Supplement Fig. S3 shows results with $\lambda = 4$. This larger source rate leads to faster early gelation in the support region and also wider spread of oligomers outside of this region because of steep concentration gradients. At times $t \geq 2$, with the source largely exhausted, continued gelation within the source region depletes oligomers there and results in substantial reverse diffusion. The result at $t = 10$ is a taller gel profile that is almost entirely contained within the source region.

3.4.2. Variations in Branching Rate k_b.—

Here, we fix $\lambda = 1$ and consider $k_b = 1$, 4, and 16. Fig. 13a shows the propagation of the gel front for these values of k_b. Gelation within the source region occurs earliest for $k_b = 16$ and latest for $k_b = 1$. As for simulations with different source rates λ, the early occurence of gelation near $x = 0$ for a particular k_b does not imply that the gel front reaches the boundary first for that k_b. Here, the gel front for $k_b = 4$ crosses that for $k_b = 16$ and reaches the boundary significantly sooner than for the larger k_b.

Fig. S4 and Fig. S5 in the Supplement show snapshots of simulations with $k_b = 16$ and $k_b = 1$, respectively. They can be compared to those in Fig. 12 for which $k_b = 4$. Gelation near $x = 0$ occurs earliest for $k_b = 16$, and later gel growth is also much more rapid than for smaller k_b. The spatial extent of significant gelation is narrowest for $k_b = 16$ and broadens progressively as k_b decreases. At $t = 10$, the values of θ_g at $x = 0$ increase approximately four-fold and those at the boundary decrease by more than 16-fold as k_b increases from 1 to 16. Similarly B_g at $x = 0$ increases substantially as k_b increases. The reverse gradients in B_s and θ_s are more pronounced for $k_b = 16$ than for $k_b = 4$, and are nonexistent or weak for $k_b = 1$. At $t = 10$, f^A is a little above 2 throughout the domain for all k_b, and as k_b increases, the structure parameter B/θ increases for all x and it has a higher "bump" for smaller $|x|$, where the gel is concentrated, for large k_b.

3.4.3. Variations in Diffusivity D and D_1.—Fig. 13b shows gel front propagation for simulations in which monomers and oligomers diffuse and D was varied over the values $D = 0.16, 0.04, 0.01$, while $\lambda = 1$ and $k_b = 4$. Near $x = 0$, gelation occurs earlier for smaller D, and the front propagates towards larger $|x|$ much more rapidly for $D = 0.16$ and $D = 0.04$ than for $D = 0.01$. The solution snapshots in Supplement Figs. S6–S7 for $D = 0.16$ and $D = 0.01$, respectively, can be compared to those in Fig. 12 for which $D = 0.04$. No gel formation is apparent up to $t = 0.5$ for $D = 0.04$ and $D = 0.16$, while $\theta_g(0,0.5) > 1$ for $D = 0.01$. For $D = 0.16$, sol has spread throughout the domain by $t = 0.5$, and there is little sign of reverse gradients at this or later times. When gelation does ensue, it does so over the entire domain with only moderately higher θ_g and B_g levels near $x = 0$ than near the boundary. In contrast, for $D = 0.01$, reverse gradients in sol quantities develop near the source by $t = 2$ and throughout the domain by $t = 10$, and gelation is confined to a narrow region around $x = 0$ during the entire simulation. The sturcture variables vary notably in space. Due to the rapid growth of the gel near $x = 0$ by $t = 0.5$, the average functionality f^A there has already begun to drop. It is highest in locations adjacent to the gel to which sol has spread but not yet gelled; it remains high where little gelation occurs.

Next, we consider simulations in which only monomer diffuses. The necessary modifications to the PDEs are described in Supplement section S1.2. Fig. 13c shows gel front propagation for monomer diffusion coefficient $D_1 = 0.16, 0.04, 0.01$ with $D = 0$. Comparing these gel fronts to those in Fig. 13b, we see earlier gelation at $x = 0$, slower movement of the gel front across the source region, and much slower propagation of the front from the edge of the source to the boundary. In fact, only for $D_1 = 0.16$ does the front come close to the boundary by the end of the simulation. These behaviors are all due to the immobility of the oligomers, which allows faster progression in oligomer size near $x = 0$ while hindering this progression elsewhere.

Supplement Figs. S8 and S9 show snapshots of the dynamics for $D_1 = 0.04$ and $D_1 = 0.16$, respectively. For $D_1 = 0.04$, gelation is underway near $x = 0$ before $t = 0.5$. By $t = 10$, the gel peak has grown and the spatial extent of the gel has widened somewhat, but is confined to $|x| < 0.25$. For the simulation in Fig. 12, in which oligomers also diffuse, the peak is a little lower and the gel front has reached the boundary by $t \approx 1.5$. With only monomer diffusing, θ_s and R_s are much higher immediately adjacent to the gel front (see Fig. S8d) than farther away or than when oligomer also diffuses (see Fig. 12djp). f^A in Fig. S8cfi drops to near 2 within most of the gel but is high adjacent to it, exceeding 3 at $t = 10$. The sol concentrations there are low, but high f^A suggests that further branch formation will occur there. For $D_1 = 0.16$ (Fig. S9, compare with Fig. S6), the gel grows faster and to a higher peak near $x = 0$ than when oligomers also diffuse, but at $t = 2$ it is confined to the region $|x| < 0.25$, whereas it reaches the boundary shortly after $t = 1$ if oligomers also diffuse. By $t = 10$, gelation has spread all the way to the boundary, but θ_g near the boundary is only about 40% of that when oligomers diffuse. At $t = 10$, f^A and B/θ are distributed heterogeneously when $D = 0$ and $D_1 = 0.16$ compared to their almost uniform distribution when $D = D_1 = 0.16$.

4. Discussion.

In this paper, we consider a model of fibrin polymerization that investigates the spatial and temporal behavior of the polymers both pre- and post-gelation. Using the framework we introduced in [9], we study the early behavior of the system using moment equations derived from a doubly-infinite set of ODEs that describe the oligomer concentrations. The moment equations are valid only until gel time which is when a second moment, tracked by these equations, blows up. As we did in [10] for a simpler kinetic gelation model, we develop an alternative approach, based on the generating function of the oligomer concentrations, in order to extend our studies past gel time. To do this, we make assumptions about the types of reactions in which the gel can particpate, and use them to derive a closed system consisting of a PDE for the generating function and an ODE for the reaction site density. We find that the new system produces behaviors that agree with the moment system prior to gel time and it lets us continue our studies after gelation. We examine our assumptions about post-gelation reactions using the Gillespie method to carry out stochastic simulations beginning with a large, but finite, set of discrete monomers. These simulations agree with the solutions to the original differential equation system before gelation and with the new PDE system after gelation, giving support to our assumptions about post-gelation reactions. Finally, we extended the PDE system by incorporating spatial heterogenity and transport in space by diffusion.

The essential kinetic processes in our model are linking reactions, in which two oligomers join together without formation of a new branch, and branching reactions, in which three oligomers join together to form a new branch. These processes have timescales $1/(k_l C_0)$ and $1/\left(k_b C_0^2\right)$, respectively, that are determined from their respective rate coefficients and a characteristic concentration C_0. Another time scale λ^{-1} comes from the monomer source Eq. 3.1, which models the conversion of fibrinogen by thrombin into fibrin monomers. In problems with diffusion, a fourth time scale is L^2/D where L is the half-width of the physical domain, and D is the diffusion coefficient. We use the linking timescale to non-dimensionalize the model equations and investigate the effects of varying the other times scales by changing λ, k_b, and D.

An important quantity in kinetic gelation models is the functionality, f. In the Ziff–Stell model, each monomer has f reactive sites and it is necessary that $f > 2$ in order for a gel to form. In our model, $f = 2$ for fibrin monomers and the number of available reaction sites in an oligomer is always two more than the number of branches in that oligomer. Since the average number of branches per oligomer is a dynamic quantity, the average oligomer functionality, f^A, is also dynamic and can increase only through branch formation. How rapidly f^A grows from its initial value influences the time until gelation and the structure of the resulting gel, and is itself affected by the relative time scales of the linking, branching, source, and diffusion processes.

We used the PDE model first in a spatially homogeneous situation and investigated the system's behavior, for different initial fibrinogen concentrations, m_0, as the rates of conversion of fibrinogen to fibrin, λ, and branching, k_b, were varied. We saw that gels form sooner for larger values of any of these parameters and that there are ranges of λ and k_b

values for which the branch point density at t_{gel} is a large fraction of the gel's branch point density after reactions have ceased, as seen experimentally [1, 4, 5]. For other values of these parameters, the branch point densities at t_{gel} and the final time are very different. A possible explanation for this is the absence from the model of fiber thickening reactions after t_{gel} which would remove oligomers from the pool that can form new branches, and thus reduce post-gel branch formation.

We then looked at how $B_s(t_{gel})$ and $f^A(t_{gel})$ vary with λ and k_b and saw that both are non-monotonic functions of k_b. To understand this behavior we turned to the moment system since the behavior of interest here occurs before gel time, and we simplified the investigation by using a source rate that is constant in time. Numerically, we found that, for each source rate, $B_s(t_{gel})$ scaled like $k_b^{-1/3}$ for $k_b \gg 1$ and like $k_b^{1/2}$ for $k_b \ll 1$. The cross-over in these scaling behaviors for intermediate k_b values explains the non-monotonicity we observed. We presented an asymptotic explanation of the two scaling behaviors, in which the reaction site density R_s, governed by Eq. 2.10, was taken to be in steady-state with a balance between source rate and link formation rate for $k_b \ll 1$ and between source rate and branching rate for $k_b \gg 1$.

Next we looked at the model in a one-dimensional spatial domain $[-L, L]$ with a time-dependent source, Eq. 3.12, limited to a narrow interval around $x = 0$. A higher value of λ or k_b or a value of D led to earlier gelation at $x = 0$, but not necessarily faster propagation of the gel front from the source to the boundary. We also see cases in which the gel's final branch point density at a particular location is lower than the earlier peak sol branch point density at the same location. These behaviors can be ascribed to diffusion carrying oligomers away from that location to other locations closer to the source, before they can become part of the gel. The "reverse gradient" driving this flux is set up when extensive gelation at locations closer to the center of the source reduces the soluble oligomer density to a sufficiently low value.

Two distinct patterns of spatial-temporal gel development are seen. For large λ or k_b or small D (see Fig. S3, S4, S7) the gel is highly peaked and largely confined to a narrow region surrounding the center of the source. In these cases, we see early reverse diffusion of oligomers, average functionality f^A that decreases towards 2 within the narrow gel while remaining high (> 2.5) adjacent to it, and structure parameter B/θ that is substantially higher within the gel than outside of it. For small λ or k_b or large D (see Fig. S2, S5, S6), we see a wide gel with a low peak, f^A that rises and then decreases towards 2 approximately uniformly in space, and a uniformly low structure parameter. Thus, a relatively large source rate or branching rate leads to a tightly confined gel, while a relatively large diffusivity leads to a dispersed one.

Our current model of fibrin polymerization model does have limitations. We make specific simplifying assumptions about diffusion of oligomers of different sizes. This is done (i) to produce a mathematically tractable treatment of diffusion and (ii) because for the *in vivo* situations to which we will ultimately apply the model (after we couple it to our existing models of platelet deposition and coagulation under flow [7, 15, 17]), there are two cases of particular interest, in both of which diffusion of large oligomers is expected to be of

limited importance. If a clot forms inside a blood vessel, advection is generally dominant over diffusion and we would expect many small fluid-phase oligomers to be washed away before they combine into large oligomers, and it may be that only the fibrin strands which are anchored to platelets remain at the injury site. On the other hand, if a clot forms in the complex milieu of the extravascular space (in the presence of cells and extracellular protein matrices), the spatial gaps in which molecules can diffuse are likely to be small, and this would reduce the importance of diffusion of large oligomers. Another limitation of the current model is that it does not treat fiber thickening after gel time, which is seen to be important experimentally [22, 21] and extending the model to treat thickening is an open question. The model also does not account for the fact that fibrinogen can bind to a fibrin oligomer and, until that fibrinogen is converted to fibrin, reduce the ability of that oligomer to bind with other oligomers. In [18], we present our preliminary work on analyzing models of polymerization that involve two types of monomers. A paper using similar ideas to include fibrinogen binding in the fibrin branching model is forthcoming. An open issue is the coupling of our fibrin polymerization model with our existing non-spatial [14, 7, 15, 17] and spatial [16] models of coagulation biochemistry and platelet deposition under flow. Fibrinogen will be converted to fibrin by thrombin at the concentrations that emerge from the calculations, fibrinogen and fibrin in the plasma will be transported with the flow, and we expect that the binding of fibrinogen and fibrin to the surfaces of platelets in the clot will play an important role in the dynamics.

Supplementary Material

Refer to Web version on PubMed Central for supplementary material.

Acknowledgments.

This work was supported in part by NSF grant DMS-1716898 and NHLBI grant R01HL151984 to ALF and by a grant to ACN from BioFire Diagnostics.

REFERENCES

[1]. Blombäck B, Carlsson K, Fatah K, Hessel B, and Procyk R, Fibrin in human plasma: Gel architectures governed by rate and nature of fibrinogen activation, Thromb Res, 75 (1994), pp. 521–538. [PubMed: 7992253]

[2]. Campbell RA, Overmyer KA, Bagnell CR, and Wolberg AS, Cellular procoagulant activity dictates clot structure and stability as a function of distance from the cell surface, Arter Thromb Vasc Biol, 28 (2008), pp. 2247–2254.

[3]. Campbell RA, Overmyer KA, Selzman CH, Sheridan BC, and Wolberg AS, Contributions of extravascular and intravascular cells to fibrin network formation, structure, and stability, Blood, 114 (2009), pp. 4886–4896. [PubMed: 19797520]

[4]. Chernysh IN, Nagaswami C, and Weisel JW, Visualization and identification of the structures formed during early stages of fibrin polymerization, Blood, 117 (2011), pp. 4609–4614. [PubMed: 21248064]

[5]. Chernysh IN and Weisel JW, Dynamic imaging of fibrin network formation correlated with other measures of polymerization, Blood, 111 (2008), pp. 4854–4861. [PubMed: 18272815]

[6]. Collet J, Park D, Lesty C, Soria J, Soria C, Montalescot G, and Weisel J, Influence of fibrin network conformation and fibrin fiber diameter on fibrinolysis speed: dynamic and structural approaches by confocal microscopy, Arter Thromb Vasc Biol, 20 (2000), pp. 1354–1361.

[7]. Elizondo P and Fogelson A, A model of venous thrombosis initiation, Biophys J, 111 (2016), pp. 2722–2734. [PubMed: 28002748]

[8]. Fatahl K, Silveiro A, Tornval P, Karpeo F, Blomböck M, and Hamsteno A, Proneness to formation of tight and rigid fibrin gel structures in men with myocardial infarction at a young age, Hypertension, 7 (1996), p. 2.

[9]. Fogelson AL and Keener JP, Toward an understanding of fibrin branching structure, Physical Review E, 81 (2010), p. 051922.

[10]. Fogelson AL and Keener JP, A framework for exploring the post-gelation behavior of Ziff and Stell's polymerization models, SIAM J Appl Math, 75 (2015), pp. 1346–1368. [PubMed: 30774159]

[11]. Fogelson AL and Neeves KB, Fluid mechanics of blood clot formation, Ann Rev Fluid Mech, 47 (2015), pp. 377–403. [PubMed: 26236058]

[12]. Gillespie DT, A general method for numerically simulating the stochastic time evolution of coupled chemical reactions, J Comput Phys, 22 (1976), pp. 403–434.

[13]. Guy R, Fogelson A, and Keener J, Fibrin gel formation in a shear flow, Math Med Biol, 24 (2007), pp. 111–130. [PubMed: 17018571]

[14]. Kuharsky AL and Fogelson AL, Surface-Mediated Control of Blood Coagulation : The Role of Binding Site Densities and Platelet Deposition, Biophysical Journal, 80 (2001), pp. 1050–1074. [PubMed: 11222273]

[15]. Leiderman K, Chang W, Ovanesov M, and Fogelson A, Synergy between Tissue Factor and Factor XIa in initiating coagulation, Arter Thromb Vasc Biol, 36 (2016), pp. 2334–2345.

[16]. Leiderman K and Fogelson AL, Grow with the flow: A spatial-temporal model of platelet deposition and blood coagulation under flow, Mathematical Medicine and Biology, 28 (2011), pp. 47–84. [PubMed: 20439306]

[17]. Link K, Stobb M, Sorrells M, Bortot M, Ruegg K, Manco-Johnson M, Paola JD, Sindi S, Fogelson A, Leiderman K, and Neeves K, A mathematical model of coagulation under flow identifies factor V as a modifier of thrombin generation in hemophilia A, J Thromb Hemost, 18 (2020), pp. 306–317.

[18]. Nelson AC, Keener JP, and Fogelson AL, Kinetic model of two-monomer polymerization, Physical Review E, 101 (2020), p. 022501. [PubMed: 32168560]

[19]. Rukhlenko O, Dudchenko OA, Zlobina KE, and Guria1 GT, Mathematical modeling of intravascular blood coagulation under wall shear stress, PLOS One, 10 (2015), p. e0134028. [PubMed: 26222505]

[20]. Ryan EA, Mockros LF, Weisel JW, and Lorand L, Structural origins of fibrin clot rheology, Biophys J, 77 (1999), pp. 2813–2826. [PubMed: 10545379]

[21]. Weisel J, Structure of fibrin: Impact on clot stability, J Thromb Haemos, 5 (2007), pp. 116–124.

[22]. Weisel J and Nagaswami C, Computer modeling of fibrin polymerization kinetics correlated with electron microscope and turbidity observations: clot structure and assembly are kinetically controlled, Biophys J, 63 (1992), pp. 111–128. [PubMed: 1420861]

[23]. Weisel JW, Fibrinogen and fibrin, in Adv Prot Chem, vol. 70, Elsevier, 2005, pp. 247–299.

[24]. Wolberg AS and Campbell RA, Thrombin generation, fibrin clot formation and hemostasis, Transf Apher Sci, 38 (2008), pp. 15–23.

[25]. Zapata-Allegro CL, Mathematical Modeling of Fibrin Gelation Dynamics and Structure Formation Under Flow, PhD thesis, The University of Utah, 2018.

[26]. Ziff RM and Stell G, Kinetics of polymer gelation, J Chem Phys, 73 (1980), pp. 3492–3499.

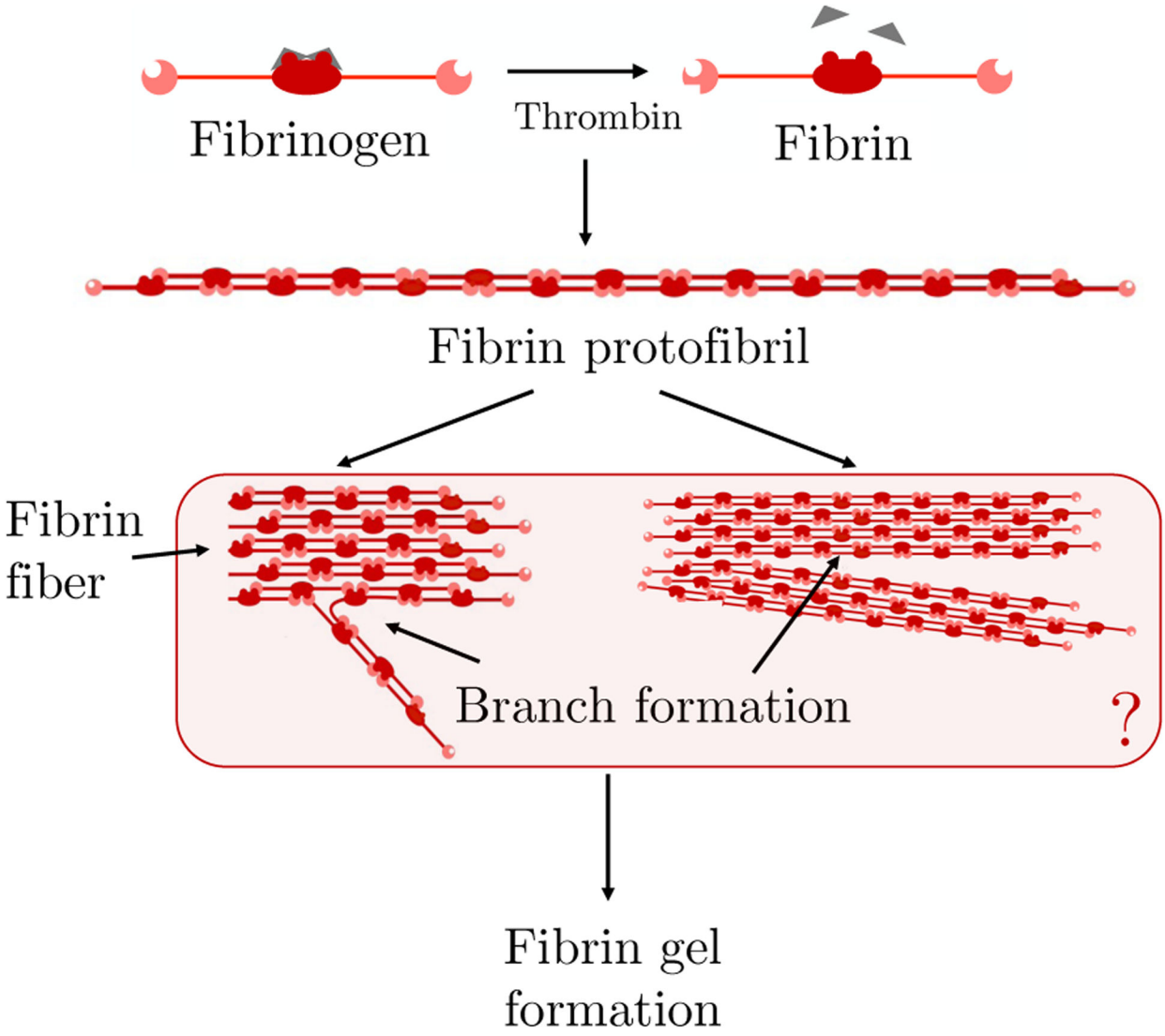

Fig. 1:
Schematic of fibrin polymerization showing thrombin-mediated fibrinopeptide release (top), protofibril formation (middle), and hypothesized [23] modes of branch formation (bottom).

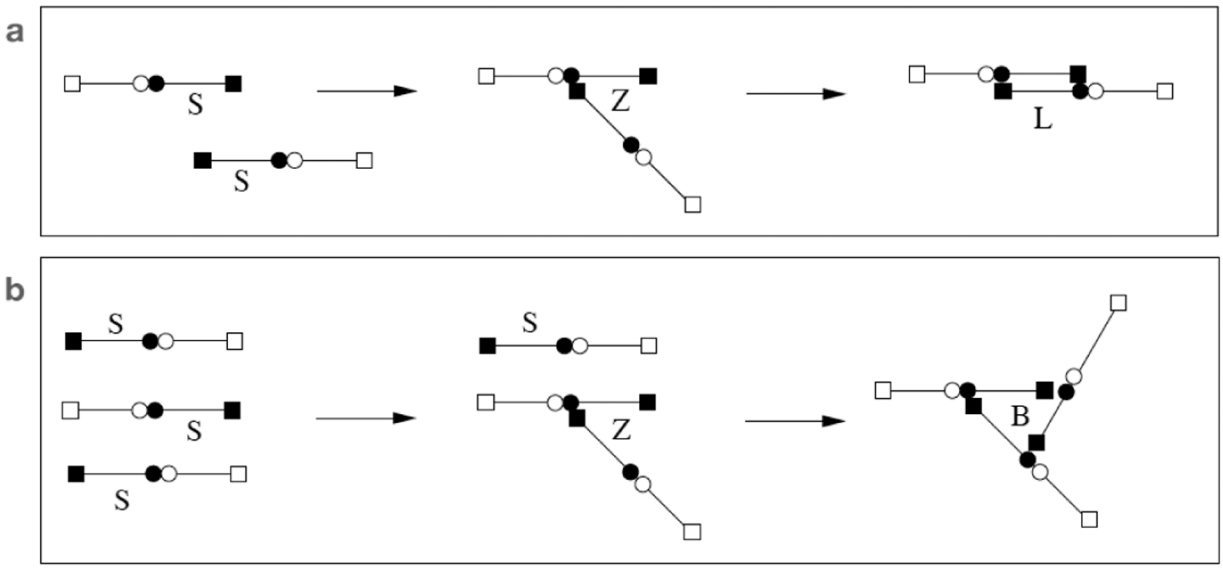

Fig. 2:
(a) Linear polymerization to form a link. (b) Branch formation.

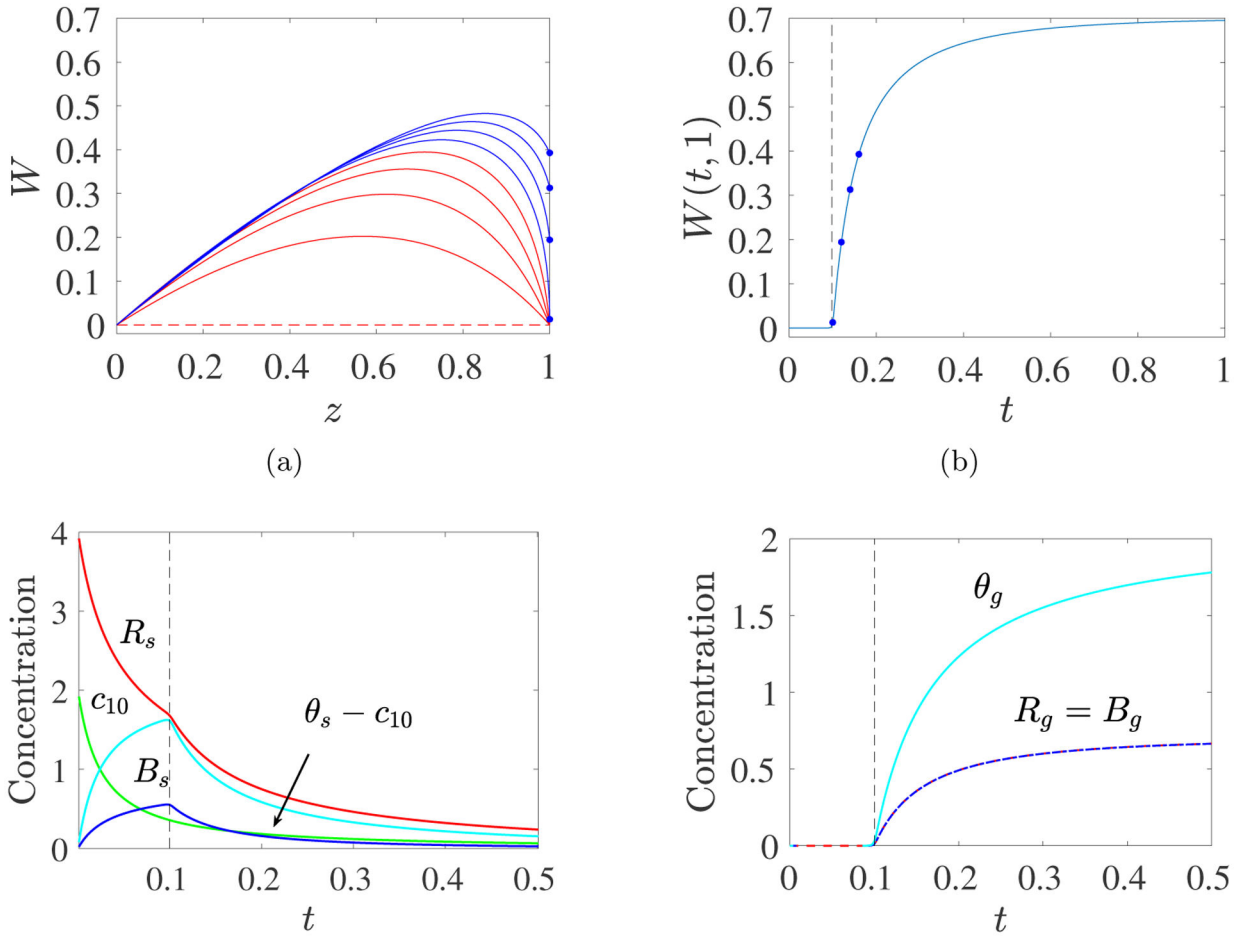

Fig. 3:

PDE Model with Spatially-uniform Initial Monomer Concentration: $c_{10}(0) = 2$, $k_l = 1$, $k_b = 2$. (a) Time snapshots of profiles $W(t, z)$ *vs* z. The curves move upward with time and are colored red before gel time and blue afterward. Values of $W(t, 1)$ for $t > t_{gel}$ are shown with dots. (b) Plot of $W(t, 1)$ *vs* t. Dots show $(t, W(t, 1))$ values corresponding to the dots in panel (a). (c) Time dependence of the concentrations of monomer c_{10}, sol reactive sites R_s, sol branches B_s, and mass in finite size oligomers larger than monomers $\theta_s - c_{10}$. (d) Time dependence of the concentrations of gel reactive sites R_g, gel branches B_g, and gel mass θ_g. Note different concentration scales in panels (c) and (d). Dashed black line indicates gel time.

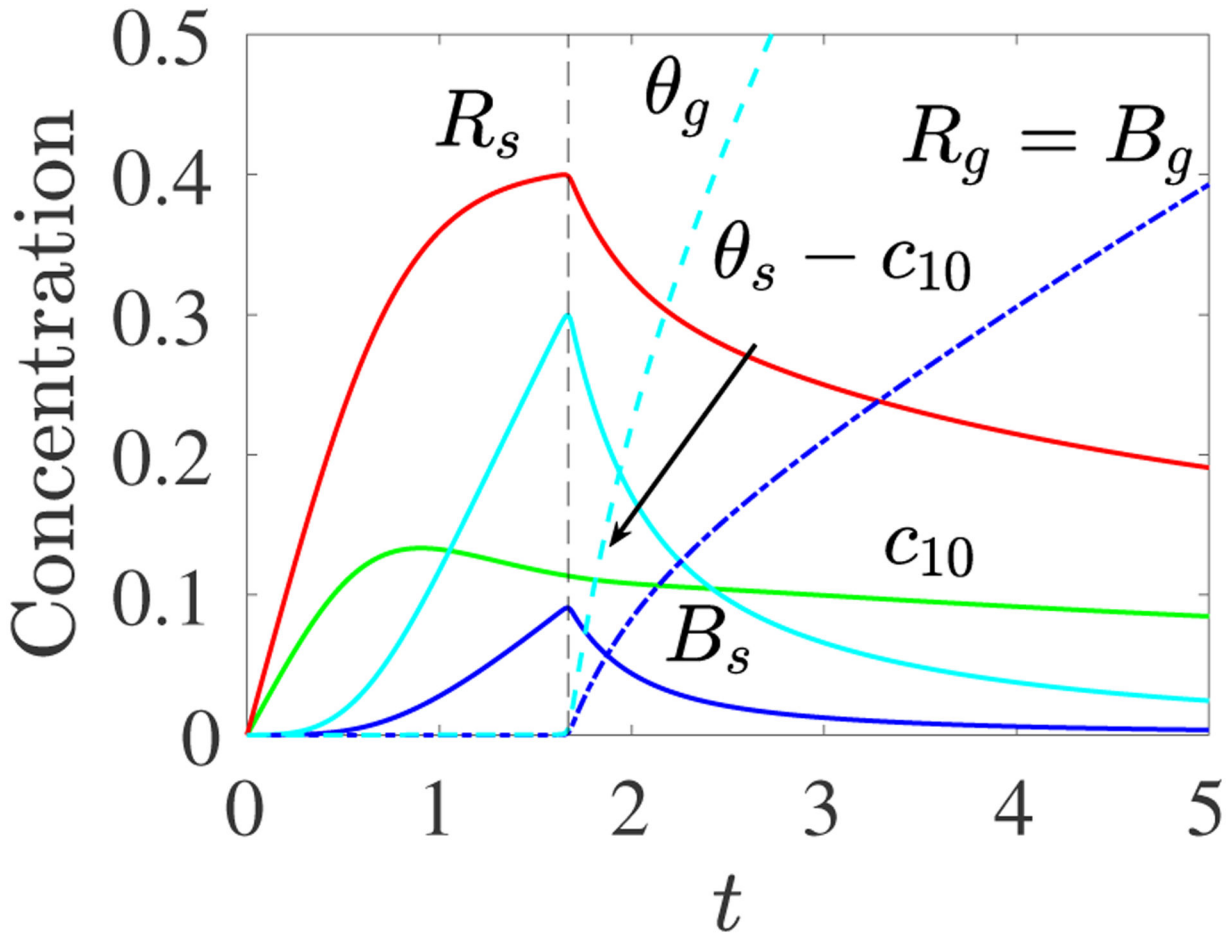

Fig. 4:

PDE Model with Spatially-uniform Monomer Source: $c_{10}(0) = 0$, $S_{10}(t) = 0.25$, $k_1 = 1$, $k_b = 10$. Plots of $c_{10}(t)$ (green), $R_s(t)$ (red), $B_s(t)$ (blue), $\theta_s(t) - c_{10}(t)$ (cyan), $R_g(t) = B_g(t)$ (dashed red and blue) and $\theta_g(t)$ (dashed cyan).

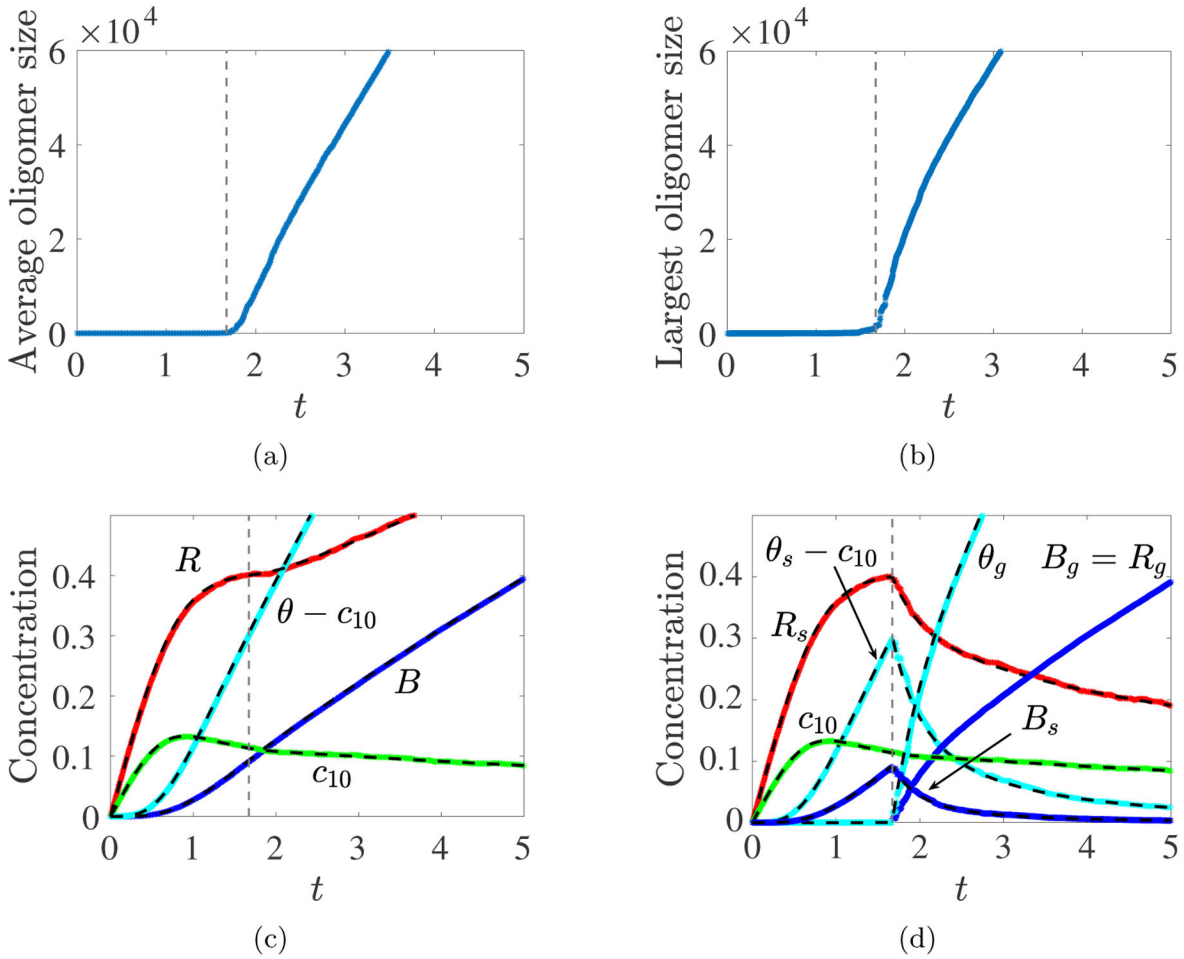

Fig. 5:

Gillespie Simulations. Rate constants $k_1 = 1$, $k_b = 10$, source rate $S_{10} = 0.25$, and volume $v = 10^5$. (a) Average oligomer size vs. t, (b) Largest oligomer size vs. t, (c) $R(t)$, $B(t)$, $\theta(t)$ and $c_{10}(t)$ from Gillespie Simulation (colors) and ODE model (dashed black) show excellent agreement up to t_{gel}. (d) After t_{gel}, the mass density (θ_g), branch point density (B_g) and reaction site density (R_g) of the largest oligomer (colors) agree well with the corresponding gel variables (dashed black) from the PDE model.

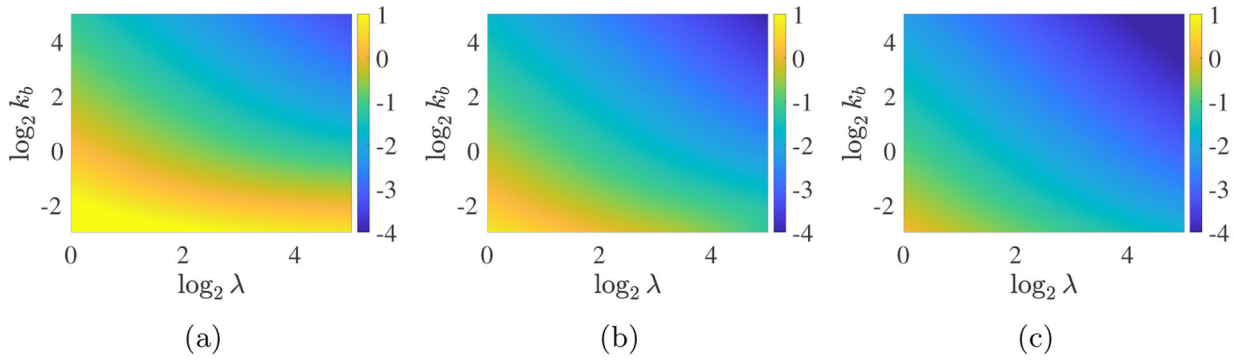

Fig. 6:

PDE Model – Gel time as a function of m_0, λ, and k_b with the spatially-uniform time-varying monomer source $S_{10} = m_0\lambda \exp(-\lambda t)$. The heatmaps show $\log_{10}(t_{gel})$ as a function of $\log_2(\lambda)$ and $\log_2(k_b)$. (a) $m_0 = 2$, (b) $m_0 = 4$, (c) $m_0 = 8$.

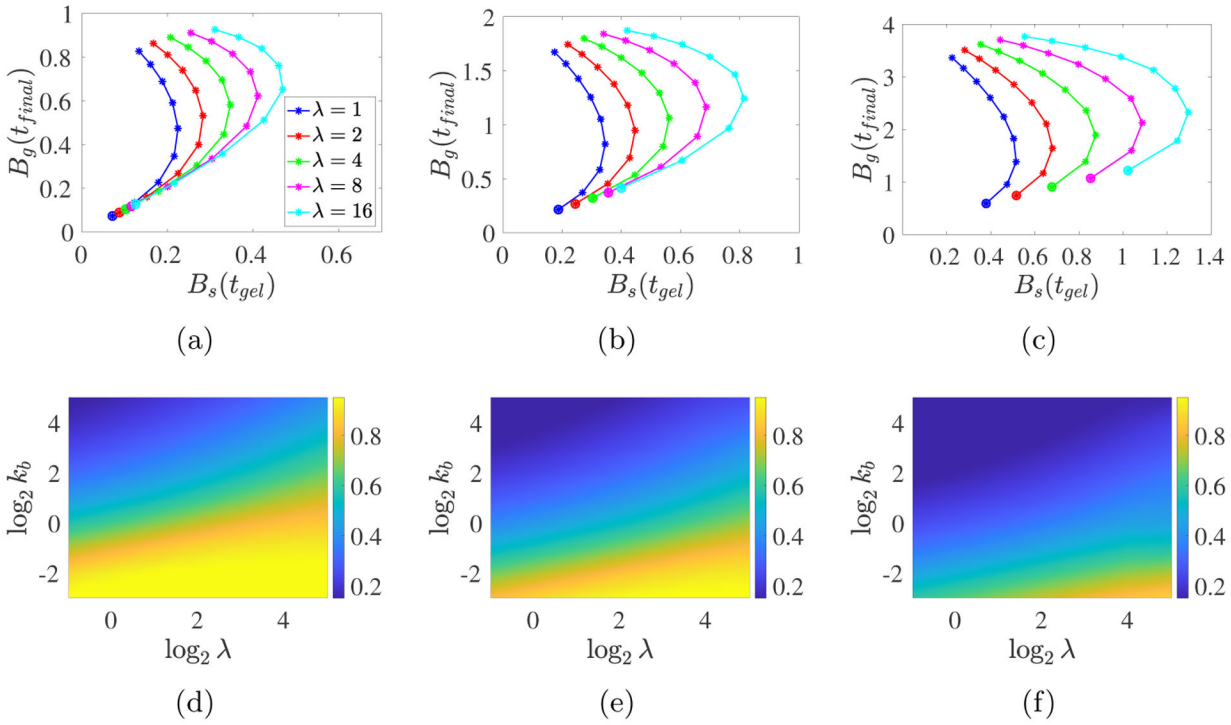

Fig. 7:

PDE model simulations with a spatially-uniform time-varying monomer source $S_{10} = m_0\lambda \exp(-\lambda t)$ for (a,d) $m_0 = 2$, (b,e) $m_0 = 4$, and (c,f) $m_0 = 8$. (a-c) Each curve corresponds to a specific λ value as indicated in the legend, and the points along each curve are for the different k_b values with the large dots indicating $k_b = 1/8$ and the k_b values increasing from that point to $k_b = 32$ at the other end of the curve. Note the different vertical scales. (d-f) The heatmaps show $B_s(t_{gel})/B_g(t_{final})$.

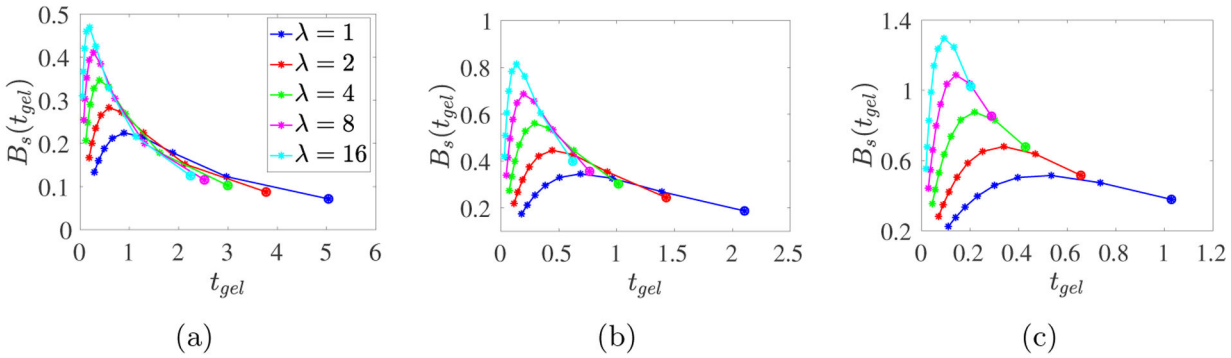

Fig. 8:

PDE model simulations with a spatially-uniform time-varying monomer source $S_{10} = m_0\lambda \exp(-\lambda t)$ for (a) $m_0 = 2$, (b) $m_0 = 4$, and (c) $m_0 = 8$. Each curve corresponds to a specific λ value as indicated in the legend, and the points along each curve are for the different k_b values with the large dot indicating $k_b = 1/8$ and the k_b values increasing from that point to $k_b = 32$ at the other end of the curve.

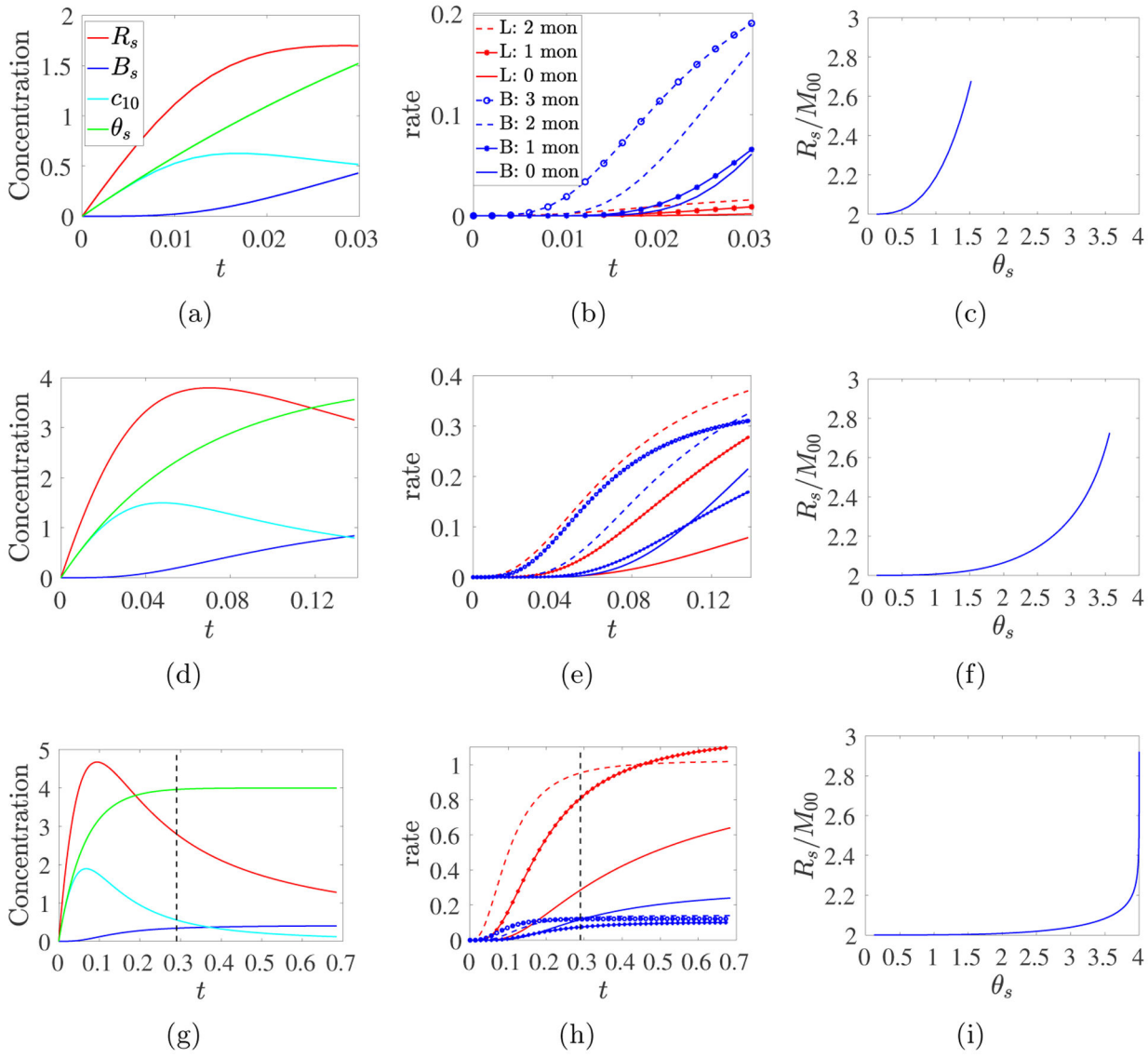

Fig. 9:

ODE model simulations with a time-dependent source $S_{10}(t) = m_0\lambda \exp(-\lambda t)$ with $m_0 = 4$ and $\lambda = 16$, and (abc) $k_b = 32$, (def) $k_b = 1$, (ghi) $k_b = 1/8$. (Left) Plots of $R_s(t)$, $B_s(t)$, $c_{10}(t)$, and $\theta_s(t)$ until $t = t_{gel}$. (Middle) Rates of link and branching formation reactions involving different numbers of monomers. (Right) Average functionality $f(t) = R_s(t)/M_{00}(t)$ vs. cumulative monomer sourced $\theta_s(t)$. Dashed black lines indicate when 99% of the monomer has been sourced.

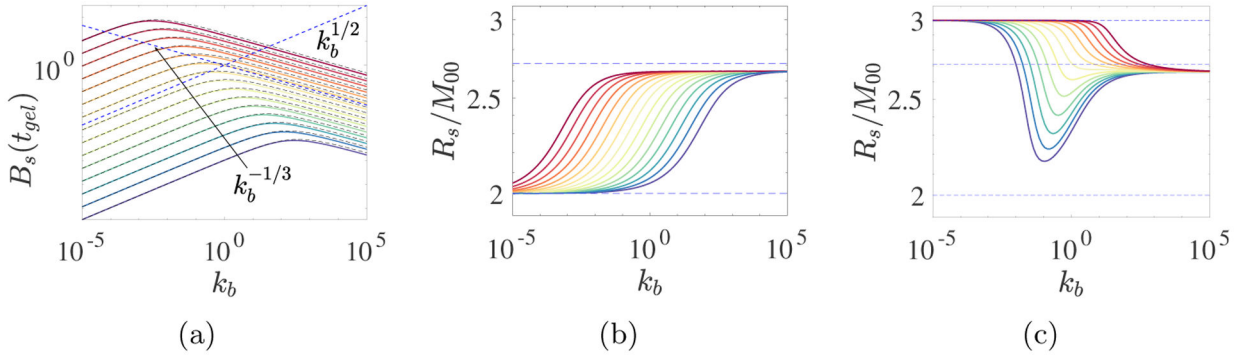

Fig. 10:

ODE model calculations for various branching rates k_b and various (a,b) constant source rates S_{10} and (c) time-varying source rates. (a) Colored curves show $B_s(t_{gel})$, blue dashed lines show its scaling behaviors, and black curves show approximate $B_s(t_{gel})$ from Eq. 3.10 using r_{ss} values computed by solving Eq. 3.5 numerically; (b) Colored curves show average functionality $f^A = R_s/M_{00}$ at t_{gel}. In (a) and (b), S_{10} decreases from 10^5 (deep red curve) to 10^{-5} (deep blue curve). Dashed blue line in (b) and (c) is $2/(1 - B_s/R_s) \approx 2.7093$ (see text). (c) Average functionality for time-varying source rate $S_{10}(t) = m_0\lambda \exp(-\lambda t)$ $m_0 = 4$ and λ decreases from 10^5 (deep red curve) to 10^{-5} (deep blue curve). Branching rates k_b vary as indicated.

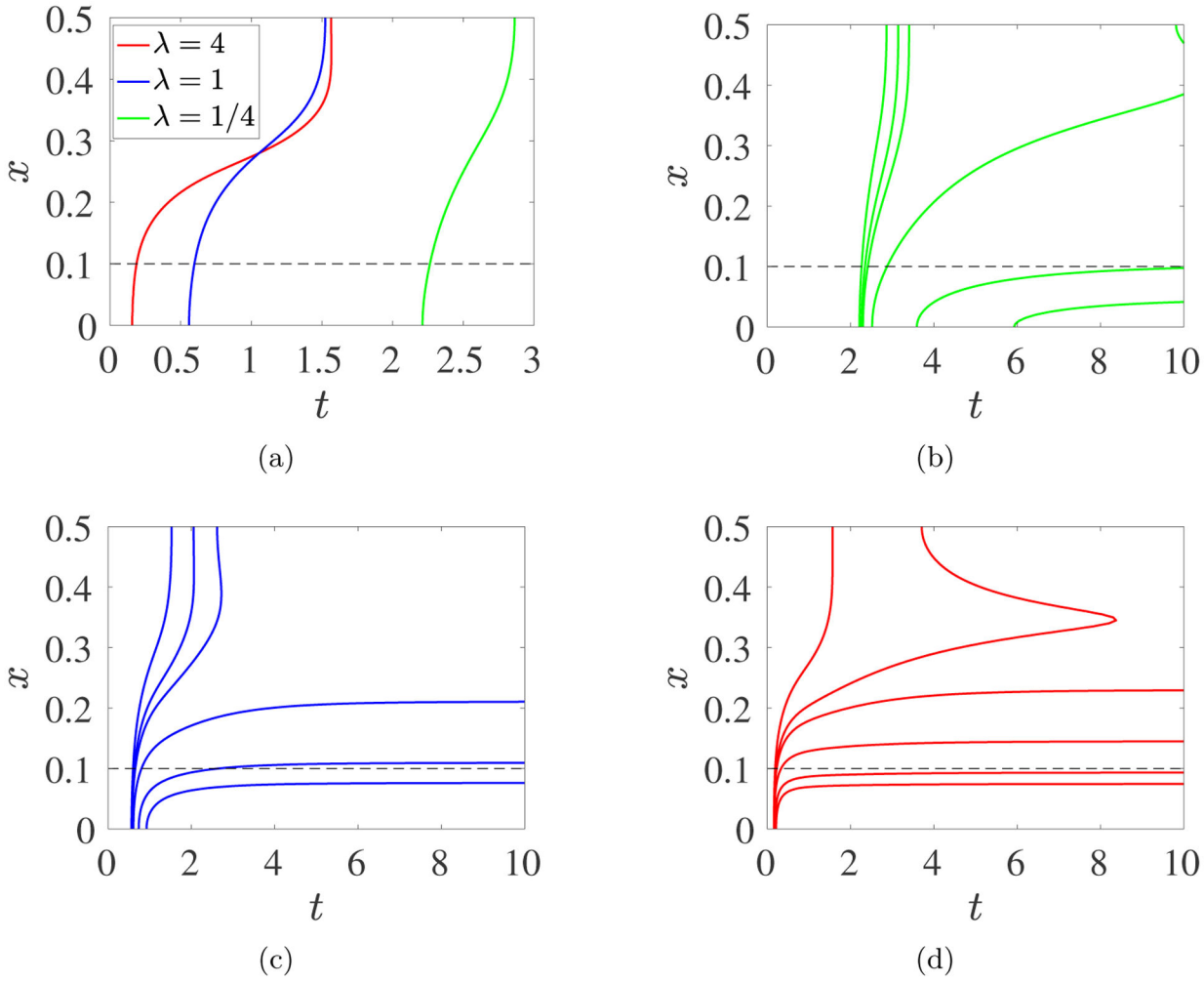

Fig. 11:

PDE model simulations with source rate $S_{10}(x, t)$ given in Eq. 3.12, with $m_0 = 8$, $k_b = 4$, $\lambda = 0.25, 1.0, 4.0$, contours of R_g in the xt–plane. (a) Contour $R_g(x, t) = B_g(x, t) = 0.001$ for $\lambda = 4.0$ (red), 1.0 (blue), and 0.25 (green). Each contour defines the gel front location $x_{gel}(t)$ vs t. (b,c,d) Contours $R_g(x, t) = B_g(x, t) = 0.001$, 0.005, 0.01, 0.05, 0.25, and 0.50 (increasing from left to right) for (b) $\lambda = 0.25$, (c) $\lambda = 1.0$, and (d) $\lambda = 4.0$. The black dashed lines show the upper edge of the monomer source's support. Note the different time interval in (a).

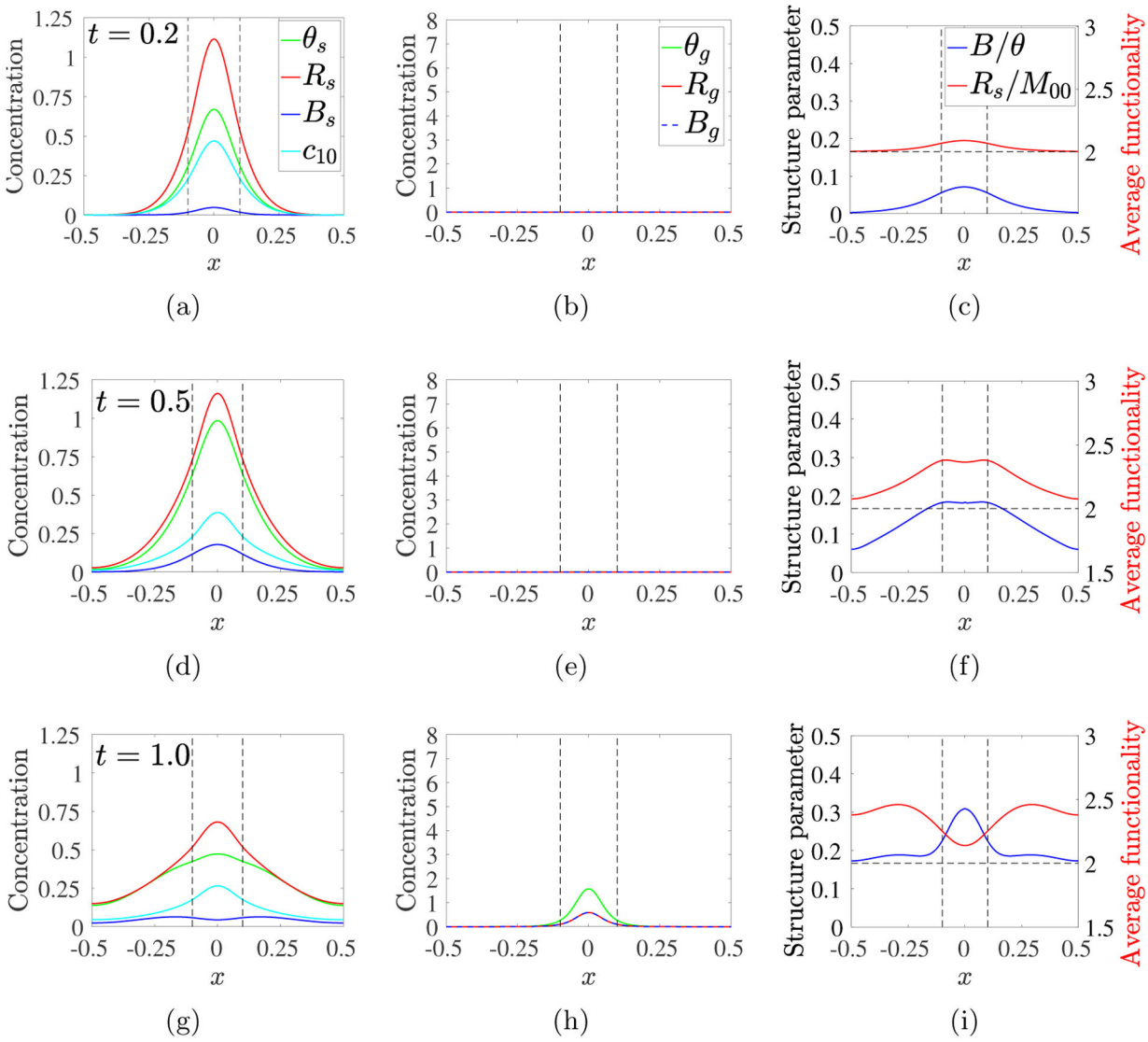

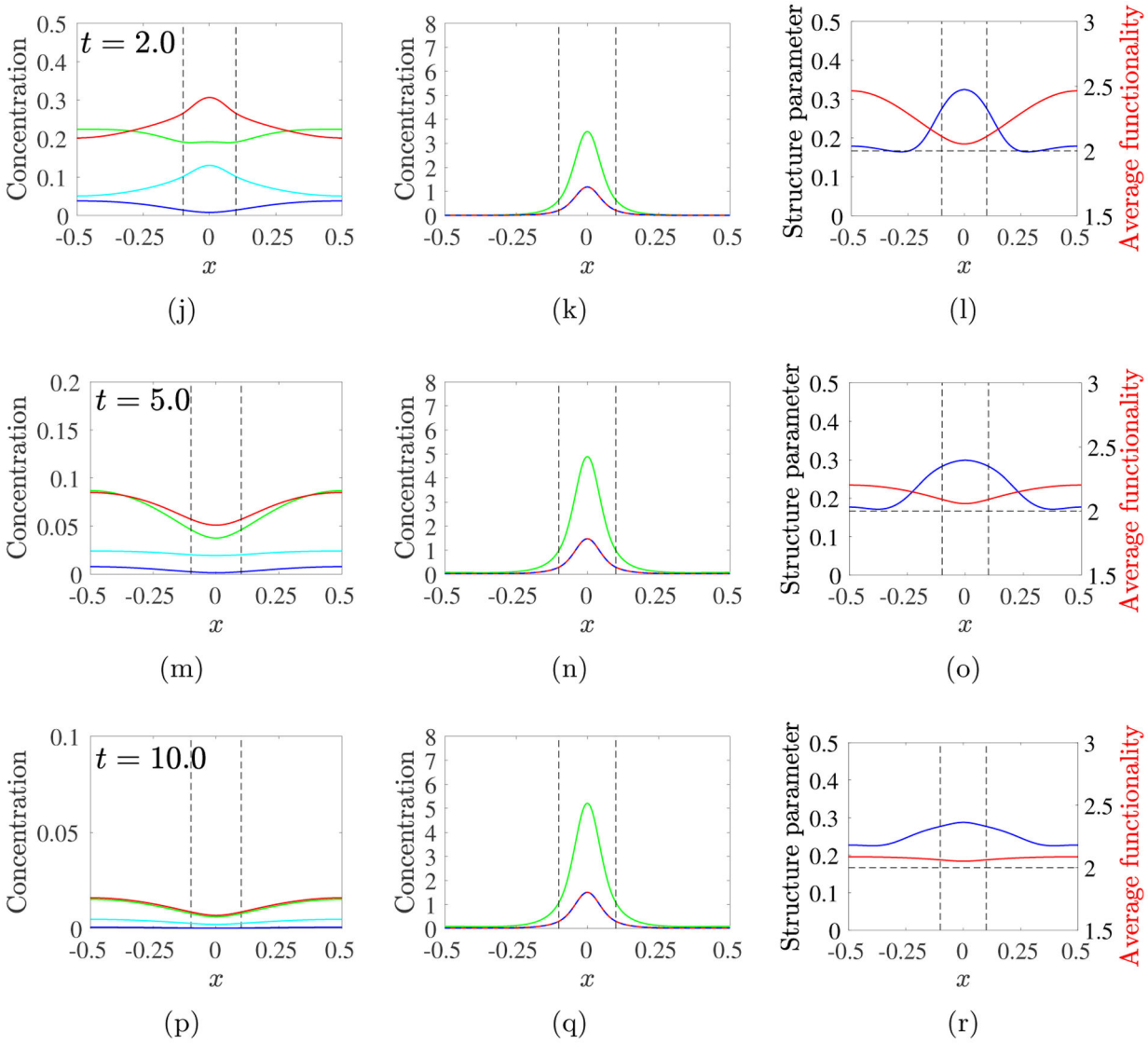

Fig. 12:

PDE model simulations with source rate $S_{10}(x, t)$ given in Eq. 3.12, with $m_0 = 8$, $k_b = 4$, $\lambda = 1$, $D = 0.04$. Snapshots of sol variables (left) gel variables (middle), and structure variables (right) at the times indicated for each row. Note change in vertical scale in left column. Black dashed vertical lines show extent of source's spatial support.

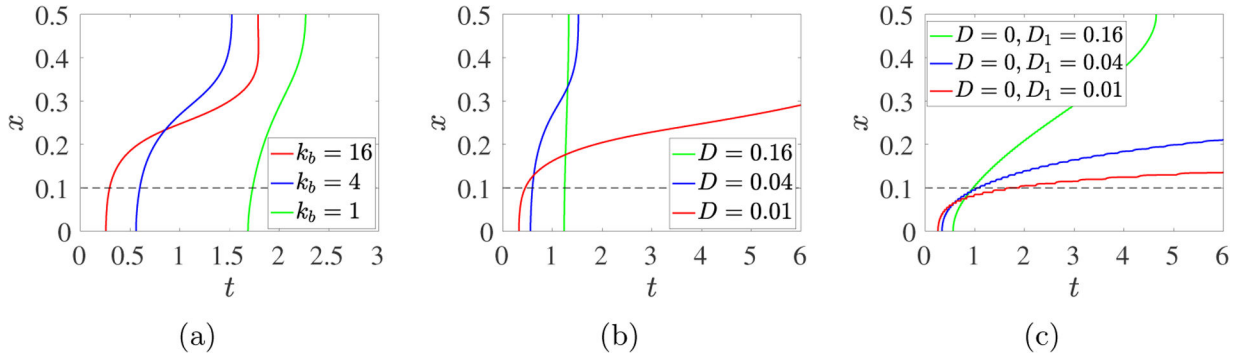

Fig. 13:

PDE model simulations with source rate $S_{10}(x, t)$ given in Eq. 3.12, with $m_0 = 8$ and $\lambda = 1$ contours of $R_g = 0.001$ in the xt–plane for (a) $D = 0.04$ and $k_b = 1, 4, 16$, (b) $k_b = 4$ and $D = 0.16, 0.04, 0.01$, (c) $k_b = 4$, $D = 0$, and $D_1 = 0.16, 0.04, 0.01$, The black dashed lines show the upper edge of the monomer source's support.